MONOLITHICALLY INTEGRATED MICRO FUEL CELLS FOR ON-CHIP POWER GENERATION

BY

PEDRO O. LÓPEZ-MONTESINOS

DISSERTATION

Submitted in partial fulfillment of the requirements
for the degree of Doctor of Philosophy in Chemical Engineering
in the Graduate College of the
University of Illinois at Urbana-Champaign, 2011

Urbana, Illinois

Doctoral Committee:

Professor Paul J.A. Kenis, Chair
Professor George H. Miley
Professor Deborah Leckband
Assistant Professor Christopher V. Rao
Assistant Professor Brendan A. Harley

Abstract

The portable technology has emerged with miniature, highly integrated consumer electronics with multi-tasking capability in part enabled by recent advances in wireless communication and data transmission. Similarly, the next generation of autonomous microelectromechanical systems (MEMS) is expected to perform in the diverse arenas of medicine, environmental sciences, and engineering. These new power demands have fostered the development of high energy density micro-fuel cells that can be integrated into these devices, while preserving their latitude and portability **(Chapter 1)**. Monolithic integration offers the possibility of cofabricating micro-fuel cells along with other electronic components on the same chip to enable overall device miniaturization, weight and cost reduction, and improved signal integrity. However, to achieve such a method of integration, the cells must be built conform to the microfabrication technologies for integrated circuits (IC) and microelectromechanical systems (MEMS) standards. Therefore, key challenges, such as the incompatibility of fuel cell materials (*e.g.,* perfluorosulfonic acid polymer membrane, carbon-based layers) with the aforementioned technologies, and integration issues must be overcome (**Chapter 2).** In this work, we present the design, fabrication, and characterization of an on-chip monolithically integrated micro-fuel cell. By omitting the integration of the proton exchange membrane (PEM), the design resulted in a planar, IC-compatible micro laminar flow fuel cell (μLFFC) suitable for on-chip power **(Chapter 3)**. The principles of any working micro-fuel cell are of strongly coupled, non-linear multiphysics nature. Therefore, the change of one operating parameter (*e.g.,* reactant concentration, flow rate) may induce a chain of physicochemical and electrochemical events that produces a non-obvious impact in overall micro-fuel cell integrity, performance, and efficiency. We have developed a fully-coupled numerical model that includes all transport processes and

electrochemical phenomena that occur within an operating micro-fuel cell. The model is useful to design, characterize, and optimize LFFCs **(Chapter 4)**. While the microfabrication lines and integration approaches presented herein have proven that laminar flow (membraneless) fuel cells can be monolithically integrated for on-chip power, the modeling efforts can predict performance upfront for step-wise design of superior cells.

Acknowledgements

The following passage expresses my most sincere gratitude to people that in some way or another contributed to the completion of this dissertation. First, I am profoundly grateful to my advisor, Professor Paul J.A. Kenis, for his guidance, patience, and support. Today, I feel privileged that he shared with me his well-deserved success and provided me with the necessary tools to accomplish my goals. Kenis, as a young, energetic, and determined Professor, not only inspired me, but made me realize the little wonders we can all do. Also, I would like to thank my thesis committee, Professors George Miley, Brendan Harley, and Christopher Rao, for their feedback and cooperation.

In addition to my mentors, I would like to thank Walter Pelton and Nipa Yossakda for their valuable input on this work, support, and encouragement. Thanks to all Kenis group members, especially Alix and Fik for their assistance in some electrochemistry related subjects.

I would like to thank Michael Hansen, Dane Sievers, and Darren Stevenson for their assistance when I worked at the Micro-Nano-Mechanical-Systems Cleanroom, Silicon IC Fabrication Laboratory, and Visualization Laboratory at the Beckman Institute for Science and Technology, respectively. They are exceptionally skilled in their areas, kind, and very helpful.

Special thanks go to Ave M. Alvarado for her caring counseling and help during my academic years at the University of Illinois at Urbana-Champaign (UIUC). I can't imagine the completion of my Ph.D. journey without her.

I would like to express my appreciation to two special friends: Manuel Avilés and Erick Rodríguez. Manuel, who I met in 2001, encouraged me to apply for the Summer Research Opportunities Program (SROP) at the UIUC. Having shared this experience with such a dreamer sparked a rainbow of strong ambitions in my life since then. Erick, who I met in 2004, a year

after I officially enrolled as a graduate student at the UIUC, remained my friend through thick and thin. Erick, as a highly competitive Ph.D. student, never afforded me the time to stay behind and always offered me kind, unconditional academic help.

I would also like to thank an elegant group of talented friends that made my grad-school experience an enjoyable and memorable one: Erick Rodríguez, Manuel Avilés, Eric Correa, Julissa Hidalgo, Jarice Rodríguez, Giselle Rodríguez, Xochitl Casillas, Mariangélica Carrasquillo, Trisha McNew, Angel Aquino, Melissa Marrero, Beatriz Pérez, and Don Kiu. *"¡Mil gracias, amigos!"*

I am appreciative of the generous financial support provided by the Diversifying Higher Education Faculty in Illinois (DFI) and Support for Under Represented Groups in Engineering (SURGE) fellowship programs.

Finally, I would like to thank my beautiful family: "Papá" (Pedro), "Mamá" (María), Griseida, Edgardo, and Wilber for their unconditional love, support, and encouragement. I thank them for keeping my spirit high and for teaching me the true meanings of respect, humbleness, hard work, motivation, and perseverance. Every one of them had the right words for me at the right time; words I will never forget; words that taught me that giving up is not an option in my life. I have been blessed to have them all. *"Y por eso y mucho más, a ustedes padres y hermanos les dedico mi tesis"*.

Pedro O. López-Montesinos
April, 2011

“A Papá, Mamá, Griseida, Edgardo, y Wilber”

Table of Contents

Chapter 1

Introduction

Small, portable consumer electronics such as mobile phones, laptop computers, personal digital assistants, and global positioning systems, have recently merged into single platforms and gained superior multitasking abilities in part enabled by major advances in wireless communication and data transmission [1]. The high resolution capability, batch production, and reproducibility accessible via microfabrication technologies for integrated circuits (IC) and microelectromechanical systems (MEMS) enable further miniaturization and integrated device sophistication in a cost effective manner [2,3]. Moreover, the next generation of MEMS, *i.e.,* sensors, actuators, and lab-on-a-chip devices, are expected to operate remotely to accomplish particular machine enhanced human endeavors in the diverse arenas of medicine, environmental sciences, and engineering [4-6]. Miniaturized secondary (rechargeable) batteries such as Ni-Cd, Li-ion, and Li-polymer, while presently powering the vast majority of portable devices, may no longer feature the necessary energy density to cope with these new power demands and required device autonomy [7]. As an alternative, MEMS-based electrochemical energy converters such as micro-fuel cells, particularly intended to operate with easily handled and stored liquid fuels (*e.g.,* methanol and formic acid), are envisioned as a possible solution due to their high energy density and efficiency, low temperature operation, quick start up, and quasi-instant recharge capability by easy reactant refilling [8-10].

1.1 Fuel Cells

Fuel cells are electrochemical devices that convert chemical energy directly into electricity for as long as fuel and oxidant are supplied [11]. The miniature versions of the polymer electrolyte membrane fuel cells (PEMFCs) (Figure 1.1) are expected to dominate the portable sector due to their high energy density and efficiency, low temperature operation, quick start up, and adequate ecological balance [8-10].

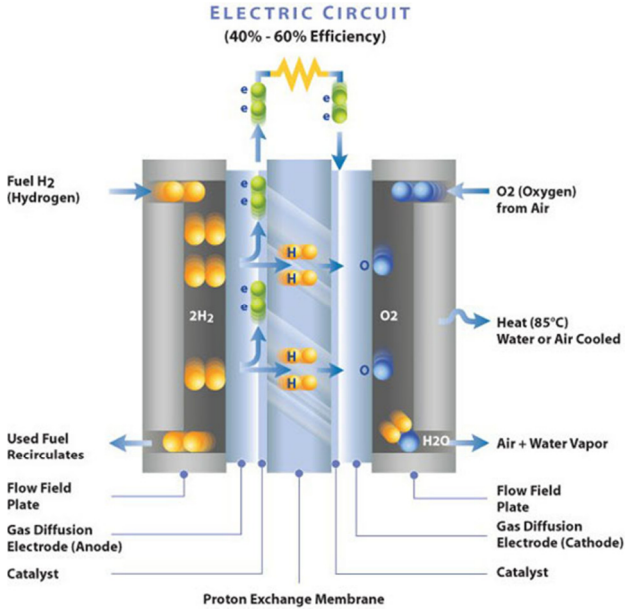

Figure 1.1. Schematic of a zero-emission hydrogen-fueled polymer electrolyte membrane fuel cell (PEMFC). At the catalyst–based anode, hydrogen electro-oxidizes and separates into protons and electrons. Freed electrons travel to the cathode via an external circuit whereas protons are transported through a proton exchange membrane (*e.g.,* Nafion). At the catalyst-based cathode, oxygen (from air) combines with protons and electrons and becomes reduced while forming water molecules. The generated water is then removed from the system by means of convection. Image courtesy of Ballard Power Systems, Inc.

For easy of miniaturization and integration, direct liquid fuel cells (DLFCs), a PEMFC category, are preferred over zero-emission hydrogen-fueled PEMFCs (Figure 1.1) or reformed hydrogen fuel cells (RHFCs) [12]. DLFCs benefit from the high energy density of many liquid

hydrocarbons (*e.g.,* methanol, ethanol and formic acid) while circumventing issues concerning hydrogen transport, compression, and storage [12]. In addition, fuel reformer (to obtain hydrogen gas from liquid hydrocarbons), gas humidification and thermal management systems are not necessary in DLFCs [12]. Furthermore, DLFCs can perform in the absence of the proton exchange membrane by feeding the liquid fuel and oxidant into a single channel at low Reynolds numbers [13-14]. This later class of DLFCs, namely, laminar flow fuel cells (LFFCs) is considered the simplest fuel cell architecture currently available in literature [10, 13-16]. The simplicity of design, minimum use of functional elements and auxiliary components for the operation of DLFCs and LFFCs has attracted researchers to pursue their miniaturization. A brief overview with respect to the design and fabrication of micro-fuel cells, specifically, DLFCs and LFFCs, is presented in the succeeding sections.

1.2 Micro-Fuel Cells: Fabrication and Integration

Fuel cells can be miniaturized using micro-electromechanical systems (MEMS) and integrated circuit (IC) processes [2-3, 17]. Due to the widespread use of Silicon in the semiconductor / portable industry, we have focused our attention in MEMS-based / Silicon-based micro-fuel cells. In general, a particular set of fabrication steps (*e.g.* photolithography, wet / dry etching, and physical / chemical deposition) may be used to shrink critical features of the fuel cell components (*e.g.,* flow fields, distribution layers, electrodes, current collectors, and membrane electrode assembly) while retaining or improving their functionality [1]. The resulting miniature cell may be a highly integrated structure with increased volumetric power density. In addition, the micro fuel cell design is intended to be as small as possible; thereby

most of the available volume is fuel. The challenge to date has been to obtain similar performance and efficiency to that of large scale fuel cells [1, 8].

1.2.1 Micro Direct Liquid Fuel Cells

Direct liquid fuel cells (DLFCs) that utilize energy-dense organic fuels such as methanol, formic acid, and ethanol have received considerable attention as energy conversion devices for portable and micro applications [12]. DLFCs are considered attractive candidates to pursue their miniaturization because they do not require a fuel reformer upstream of the cell (which greatly reduces balance of plant components and system integration) [7]. Figure 1.2 illustrates the principle of operation for a typical DLFC when operated using liquid hydrocarbons (*e.g.,* methanol, formic acid or ethanol).

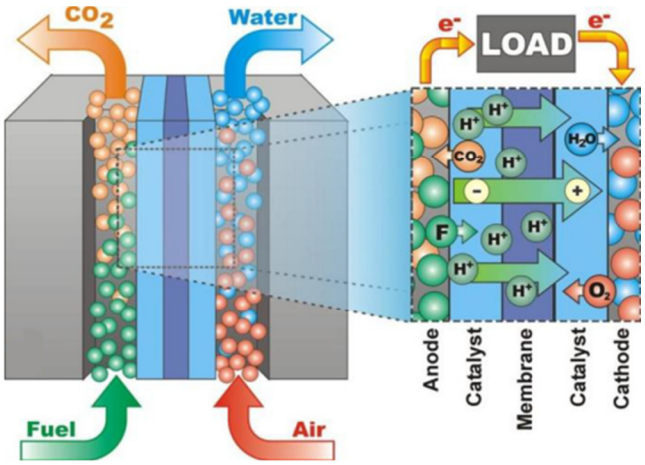

Figure 1.2. Schematic representation of a direct liquid fuel cell (DLFC). The cell utilizes small organic fuels (*e.g.*, methanol, formic acid, and ethanol). Image courtesy of Joshua Ackerman.

The majority of micro direct liquid fuel cells (μDLFCs) developed to date are membrane-based systems of bipolar architecture. Characteristically, the structure is composed of two polar

plates for the delivery of reactants and current collection, sandwiching a membrane and clamped to form a membrane electron assembly (MEA) (Figure 1.2). In general, a combination of pattern transfer and micromachining techniques (*e.g.,* dry etching, physical and chemical vapor deposition, wet isotropic or anisotropic etching) enables the miniaturization of the fuel/oxidant delivery system as well as the deposition of electrodes [1]. Nafion, a perfluorosulphonic acid ionomer, is the most common electrolyte membrane used in MEAs due to its chemical and mechanical stability and high conductivity [18]. Alternative proton exchange membranes (*e.g.,* acid loaded porous silicon) prepared by anodic etching, have been developed to improve system integration in a batch fabrication process[19]. However, significant improvement must be done to surpass the conductivity of Nafion membranes. A ***hybrid*** integration method is required to complete these micro-fuel cells. Hybrid integration implies that individual components (*i.e.,* bipolar plates and membrane electrode assembly) are fabricated separately and assembled together into a complete device (often via hot pressing techniques) [8]. Such a method of integration hinders the batch production of cells which is desired for commercialization. Moreover, the materials often used to fabricate μDLFCs (*e.g.,* Nafion, carbon-based layers) are not compatible with Silicon-based fabrication technologies [20], as will be further discussed in Chapter 2.

Within the μDLFC category, micro direct methanol fuel cells (μDMFCs) and micro direct formic acid fuel cells (μDFAFCs), are currently considered promising candidates to replace batteries in the portable sector [12, 21]. Yet, before these two cells reach the market, key challenges must be overcome [12, 21]. For instance, μDMFCs exhibit high fuel crossover rates (through Nafion membrane), sluggish anode kinetics, CO catalyst poisoning, and water management issues which cumulatively decrease the overall power output and efficiency.

Although, μDFAFCs exhibit lower fuel crossover rates (through Nafion membrane) and improved reaction kinetics (at nominal catalyst conditions), formic acid has approximately 50% of the energy density of methanol. Nevertheless, μDFAFCs are still considered good candidates because the lower rate of fuel crossover enables these micro-fuel cells to operate at higher fuel concentrations compared to μDMFCs [12, 21].

1.2.2 Micro Laminar Flow Fuel Cells (μLFFCs)

A recent concept that greatly simplifies the micro-fuel cell architecture deserves particular attention from the stand points of miniaturization and integration involves omission of the proton exchange membrane [13-14]. These membraneless LFFCs utilize the characteristic laminar state of flow for micro-scale fluids to maintain the separation of co-flowing fuel and oxidant streams in a single micro-channel [13]. The diffusion along the interface is limited and hence fuel crossover is minimized while proton transport is excellent. To improve the proton conductivity of the liquid electrolytes, fuel (*e.g.,* methanol, formic acid) and oxidant (*e.g.* saturated oxygen, potassium permanganate) are often supported in acid solutions. The anode and cathode electrodes are typically integrated on opposing microchannel walls (refer to Figure 1.3).

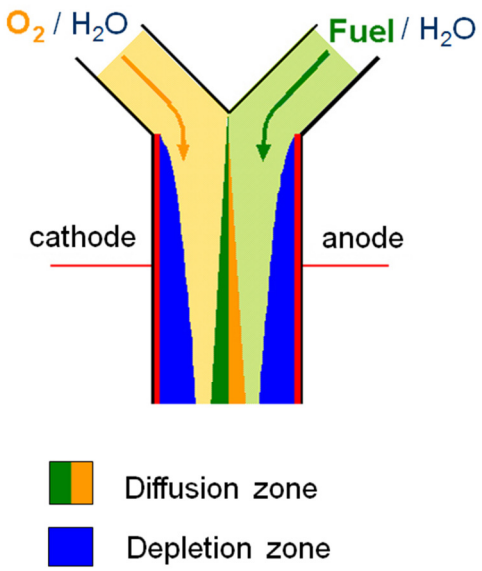

Figure 1.3. Schematic of a Y-shaped laminar flow fuel cell (LFFC). The catalyst-based electrodes are typically integrated in the opposite microchannel walls (red lines). The cell operates by flowing fuel (green) and oxidant (yellow) streams into a single microchannel at low Reynolds numbers (Re < 100). The depletion and mixing (diffusion) zones result from anode and cathode electrochemical reactions and the limited fuel-to-oxidant mixing, respectively. Image (not to scale) reprinted with the permission of Professor Paul J.A. Kenis.

The majority of LFFCs developed to date have made use of fabrication protocols already established for microfluidic chips (for analytical or lab-on-a-chip applications). Microchannels are typically fabricated by rapid prototyping, using standard and/or soft lithography techniques [22–24]. In particular, for the typical Y-shape (or T-shape) side-by-side streaming cell, the channel structures are molded in poly (dimethylsiloxane) (PDMS) and subsequently sealed to a solid substrate with the corresponding electrode patterns. Efforts to reproduce LFFCs in Silicon substrates are scarce in literature [25]. Although, LLFCs offer the simplest structural design, the fabrication and integration methods commonly used for their miniaturization do not address batch production [25]. However, the miniature LFFCs fabricated to date have served for extensive research regarding fluid dynamics, mass transport, and electrochemical phenomena to

optimize performance and efficiency. Part of this thesis is devoted to the development of highly integrated μLFFCs suitable for emerging silicon-based micro-devices.

1.3 Final Remark on the Fabrication and Integration of μDLFCs and μLFFCs

Although the miniaturization of μDLFCs and miniature LFFCs has been reported as discussed in Section 1.2, the designs may serve to power small portable devices from "*off-the-chip*" which requires significant additional latitude for installation of these power sources. For more demanding portable devices where the form factor is limited and the next generation of MEMS (*e.g.*, lab-on-a-chip devices, autonomous reconnaissance and surveillance microvehicles), on-chip integration of micro fuel cells is necessary [2, 26-27]. The focus of this thesis is to address the miniaturization and integration of DLFCs and LFFCs for on-chip power generation. On-chip integration of micro-fuel cells is covered in Chapter 2.

1.4 References

[1] Morse, J.D. 2007, "Micro-fuel cell power sources", *International Journal of Energy Research,* vol. 31, no. 6-7, pp. 576-602.

[2] Yamazaki, Y. 2004, "Application of MEMS technology to micro fuel cells", *Electrochimica Acta,* vol. 50, no. 2-3 SPEC. ISS., pp. 663-666.

[3] Kelley, S.C., Deluga, G.A. & Smyrl, W.H. 2002, "Miniature fuel cells fabricated on silicon substrates", *AICHE Journal,* vol. 48, no. 5, pp. 1071-1082.

[4] La O', G.J., In, H.J., Crumlin, E., Barbastathis, G. & Shao-Horn, Y. 2007, "Recent advances in microdevices for electrochemical energy conversion and storage", *International Journal of Energy Research,* vol. 31, no. 6-7, pp. 548-575.

[5] Flipsen, S.F.J. 2006, "Power sources compared: The ultimate truth?", *Journal of Power Sources,* vol. 162, no. 2 SPEC. ISS., pp. 927-934.

[6] Dunn-Rankin, D., Leal, E.M. & Walther, D.C. 2005, "Personal power systems", *Progress in Energy and Combustion Science,* vol. 31, no. 5-6, pp. 422-465.

[7] Kundu, A., Jang, J.H., Gil, J.H., Jung, C.R., Lee, H.R., Kim, S., Ku, B. & Oh, Y.S. 2007, "Micro-fuel cells-Current development and applications", *Journal of Power Sources,* vol. 170, no. 1, pp. 67-78.

[8] Nguyen, N. & Chan, S.H. 2006, "Micromachined polymer electrolyte membrane and direct methanol fuel cells - A review", *Journal of Micromechanics and Microengineering,* vol. 16, no. 4, pp. R1-R12.

[9] Yu, X. & Pickup, P.G. 2008, "Recent advances in direct formic acid fuel cells (DFAFC)", *Journal of Power Sources,* vol. 182, no. 1, pp. 124-132.

[10] Kjeang, E., Djilali, N. & Sinton, D. 2009, "Microfluidic fuel cells: A review", *Journal of Power Sources,* vol. 186, no. 2, pp. 353-369.

[11] O'hayre, R., Cha, S.-W., Colella, W. & Prinz, F.B. 2006, *Fuel Cell Fundamentals*, John Wiley.

[12] Demirci, U.B. 2007, "Direct liquid-feed fuel cells: Thermodynamic and environmental concerns", *Journal of Power Sources,* vol. 169, no. 2, pp. 239-246.

[13] Ferrigno, R., Stroock, A.D., Clark, T.D., Mayer, M. & Whitesides, G.M. 2002, "Membraneless vanadium redox fuel cell using laminar flow", *Journal of the American Chemical Society,* vol. 124, no. 44, pp. 12930-12931.

[14] Choban, E.R., Markoski, L.J., Stoltzfus, J., Moore, J.S. & Kenis, P.J.A. 2002, "Microfluidic Fuel Cells that Lack a PEM", *Power Sources Proceedings*, vol. 40, 317-320.

[13] Choban, E.R., Markoski, L.J., Wieckowski, A. & Kenis, P.J.A. 2004, "Microfluidic fuel cell based on laminar flow", *Journal of Power Sources,* vol. 128, no. 1, pp. 54-60.

[14] Markoski, L.J., Kenis, P.J.A. & Choban, E.R. 2007, Fuel cells comprising laminar flow induced dynamic conducting interfaces, electronic devices comprising such cells and method employing same, US Patent 7,252,898.

[15] Choban, E.R., Spendelow, J.S., Gancs, L., Wieckowski, A. & Kenis, P.J.A. 2005, "Membraneless laminar flow-based micro fuel cells operating in alkaline, acidic, and acidic/alkaline media", *Electrochimica Acta,* vol. 50, no. 27, pp. 5390-5398.

[16] Jayashree, R.S., Gancs, L., Choban, E.R., Primak, A., Natarajan, D., Markoski, L.J. & Kenis, P.J.A. 2005, "Air-breathing laminar low-based microfluidic fuel cell", *Journal of the American Chemical Society,* vol. 127, no. 48, pp. 16758-16759.

[17] Lee, S.J., Chang-Chien, A., Cha, S.W., O'Hayre, R., Park, Y.I., Saito, Y. & Prinz, F.B. 2002, "Design and fabrication of a micro fuel cell array with "flip-flop" interconnection", *Journal of Power Sources,* vol. 112, no. 2, pp. 410-418.

[18] Rikukawa, M. & Sanui, K. 2000, "Proton-conducting polymer electrolyte membranes based on hydrocarbon polymers", *Progress in Polymer Science (Oxford),* vol. 25, no. 10, pp. 1463-1502.

[19] Gold, S., Chu, K.-., Lu, C., Shannon, M.A. & Masel, R.I. 2004, "Acid loaded porous silicon as a proton exchange membrane for micro-fuel cells", *Journal of Power Sources,* vol. 135, no. 1-2, pp. 198-203.

[20] Xiao, Z., Feng, C., Chan, P.C.H. & Hsing, I.-. 2008, "Monolithically integrated planar microfuel cell arrays", *Sensors and Actuators, B: Chemical,* vol. 132, no. 2, pp. 576-586.

[21] Rice, C., Ha, S., Masel, R.I., Waszczuk, P., Wieckowski, A. & Barnard, T. 2002, "Direct formic acid fuel cells", *Journal of Power Sources,* vol. 111, no. 1, pp. 83-89.

[22] McDonald, J.C., Duffy, D.C., Anderson, J.R., Chiu, D.T., Wu, H., Schueller, O.J.A. & Whitesides, G.M. 2000, "Fabrication of microfluidic systems in poly(dimethylsiloxane)", *Electrophoresis,* vol. 21, no. 1, pp. 27-40.

[23] Xia, Y. & Whitesides, G.M. 1998, "Soft lithography", *Annual Review of Materials Science,* vol. 28, no. 1, pp. 153-184.

[24] Duffy, D.C., McDonald, J.C., Schueller, O.J.A. & Whitesides, G.M. 1998, "Rapid prototyping of microfluidic systems in poly(dimethylsiloxane)", *Analytical Chemistry,* vol. 70, no. 23, pp. 4974-4984.

[25] Tominaka, S., Ohta, S., Obata, H., Momma, T. & Osaka, T. 2008, "On-chip fuel cell: Micro direct methanol fuel cell of an air-breathing, membraneless, and monolithic design", *Journal of the American Chemical Society,* vol. 130, no. 32, pp. 10456-10457.

[26] Frank, M., Erdler, G., Frerichs, H.-., Müller, C. & Reinecke, H. 2008, "Chip integrated fuel cell accumulator", *Journal of Power Sources,* vol. 181, no. 2, pp. 371-377.

[27] Moore, C.W., Li, J. & Kohl, P.A. 2005, "Microfabricated fuel cells with thin-film silicon dioxide proton exchange membranes", *Journal of the Electrochemical Society,* vol. 152, no. 8, pp. A1606-A1612.

Chapter 2

Power Sources on a Chip

"We have the chicken-and-egg thing now. The problem is you have to design the power source when you are designing the electronic component," says Paul Kohl, professor at the Center for Innovative Fuel Cell and Battery Technologies at Georgia Institute of Technology [1].

2.1 On-Chip Integrated Power Sources

The ever-increasing trends for smaller and lighter consumer electronics have stimulated the microfabrication of power sources [2-4]. The possibility of cofabricating a power source along with other electronic components on the same chip enables overall device miniaturization, weight and cost reduction, and improved signal integrity with a minimum number of interconnects [5-6]. To achieve such a parallel integration, the power source must be built conform to the microfabrication technologies for integrated circuits (IC) and microelectromechanical systems (MEMS) standards [7-8].

2.2 Micro-Fuel Cells for On-Chip Power

Microfabricated fuel cells (micro-fuel cells) are considered attractive power sources for emerging portable devices due to their high energy density and efficiency, low temperature operation, quick start up, and adequate ecological balance [2-4]. As the semiconductor technology keeps advancing at a rapid pace along with remarkable functionalities, computing, and communication, smaller form factors are expected which imposes new miniaturization and integration challenges [19-20]. For instance, the concept of smart dust was proposed by

Warneke *et al*. to build an autonomous device that incorporates sensors, computation, wireless computation, and the power source in a cubic millimeter mote that can be used in a distributed sensor network [30]. On chip integration of the power source (*i.e.,* micro-fuel cells) will be beneficial in such extreme circumstances.

As already discussed in Chapter 1, DLFCs and LFFCs are considered attractive power sources particularly from the miniaturization and integration standpoints. Compared to hydrogen-fueled polymer electrolyte membrane fuel cells or reformed hydrogen fuel cells, DLFCs and LFFCs circumvent current issues concerning hydrogen transport, compression, and storage. In addition, no fuel reformer, gas humidification or thermal management systems are necessary for the operation of DLFCs and LFFCs which may enable us to achieve highly integrated archetypes upon miniaturization.

2.3 Design Considerations to Achieve On-Chip Integrated Micro-Fuel Cells

Despite remarkable advances in fuel cell and thin film technologies, efforts to integrate micro-fuel cells on a chip are scarcely documented [11-17]. This section will highlight important requirements to incorporate micro fuel cell power sources on electronic boards and briefly discuss corresponding key challenges.

2.3.1 Architecture

On-chip integration requires a remarkably compact micro-fuel cell architecture that maximizes reactant storage volume and yet is created with materials and processes sequences compatible with MEMS and IC mass fabrication constraints [5-6, 18]. However, following the novelty of the first miniature fuel cell fabricated by Kelley *et al.,* numerous researchers pursued the miniaturization of the traditional PEMFC and DLFC bi-layer design often composed of two bipolar substrates for the delivery of reactants and current collection clamped to membrane electrode assembly (MEA) [8,18] (Figure 2.1). To miniaturize such a complex multi- component structure significant deviations from MEMS and IC fabrication standards are inevitable [2].

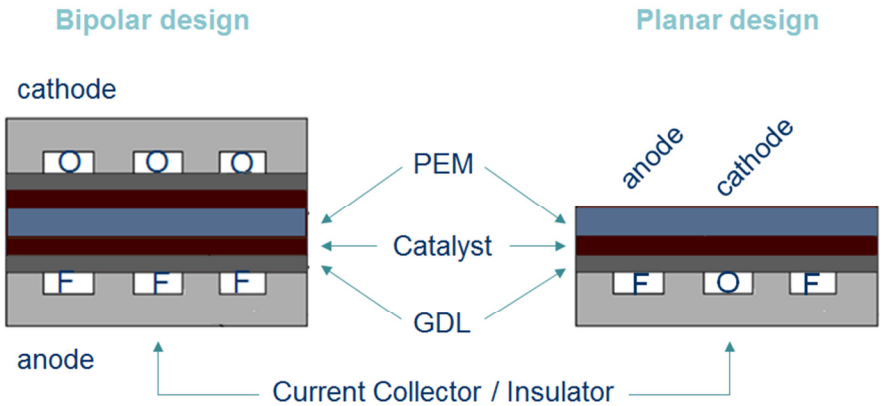

Figure 2.1. Schematic of the basic configurations of a typical micro fuel cell: (a) bi-layer design composed of two bipolar plates (anode and cathode) clamped to a membrane electrode assembly (*i.e.,* proton exchange membrane (PEM), catalyst, and gas diffusion layer (GDL)), (b) planar design with interdigitated anode and cathode compartments.

Alternatively, Mayers and Maynard, proposed a micro-fuel cell architecture with in-plane anodic and cathodic channels realized on a single silicon substrate [19] (Figure 2.1 b). Such a planar architecture is suitable for on-chip integration as all components of the fuel cell may be realized

on a single side of a substrate (*e.g.,* Silicon) which is analogous to the fabrication method for integrated circuits [2]. Such an "unfolded" planar miniature fuel cell design was mathematically modeled and proved as a less effective alternative to the bi-layer (bipolar) architecture primarily due to surface area penalties [20]. However, IC-compatible electro-deposition techniques to integrate high active surface area catalyst and surface texturing methods have been recently documented [21-23].

Remarks:

- A planar micro-fuel cell architecture may facilitate parallel integration with other electronic components on the same chip.
- All components of a planar micro-fuel cell are realized on a single side of a substrate which is analogous to the fabrication method for integrated circuits.

2.3.2 Fabrication and Integration

To achieve on-chip integrated micro-fuel cells, the overall fabrication line must be compatible with MEMS and IC batch fabrication methods [11-17].

Hybrid vs. monolithic integration

The micro-fuel cell architecture (Section 2.3.1) has a strong influence on the integration method that may be adopted to complete the system. For instance, the traditional bipolar design employed in μPEMFCs and μDLFCs is based on the stacking concept where all the components including the MEA are fabricated separately and assembled together into a complete device. Such an integration method is known as hybrid integration and deviates significantly from MEMS and IC batch fabrication standards. Conversely, a planar architecture facilitates

monolithic integration. Monolithic integration requires that all micro fuel cell components are realized on a single side of a substrate via continuous build-etch sequences analogous to the fabrication of electronic components [2]. Therefore, a monolithically integrated micro fuel cell offers the possibility of dynamic integration with other electronic components on the same chip.

"When you need something small enough to fit into a cell phone, you can't make it out of discrete parts," says Jerry Hallmark, director of energy system technologies in the Mobile Devices Technology Office of Motorola Inc. [1]

In general, two basic strategies to attain the monolithic integration of micromechanical (or microchemical) systems with their controlling electronics are the microelectronics-first (also known as CMOS-first) and micromechanics-first [24]. The process sequences to create micromechanic devices often result in high aspect ratio topologies while the fabrication of electronic components utilize high resolution photolithographic procedures that require planar substrates. The CMOS (microelectronics)-first technique (Figure 2.2) utilizes the planar nature of the substrate to achieve fine-line circuitry via photolithography and metallization procedures prior to the incorporation of micromechanical devices. However, metal-based microelectronic devices exhibit limited thermal budget. For instance, aluminum, which is traditionally used in microelectronic technologies, melts at the temperatures needed for thermal oxidation processes, doping, and specific annealing procedures for stress relaxation.

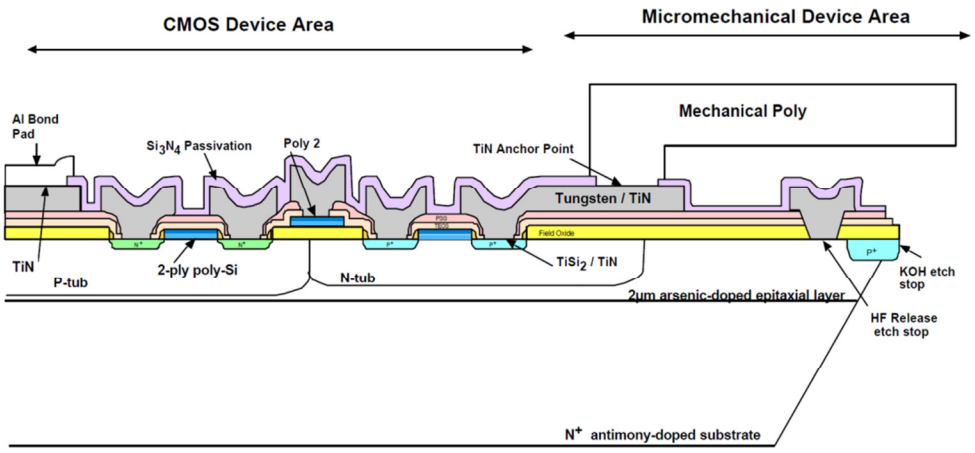

Figure 2.2. General schematic representation of the CMOS-first approach to micromechanical integration where tungsten metallization replaces the conventional aluminum metallization. Image courtesy of Sandia National Laboratories.

On the other hand, by employing micromechanics-first approach (Figure 2.3), high aspect ratio structures can be subsequently annealed, doped, or oxidized at high temperatures in the absence of metal-based microelectronics. Once micro-mechanical devices and high temperature processes are completed, the resulting topology must be planarized to incorporate microelectronic components. The micromechanics-first approach may resolve issues concerning thermal processing limitations of micro-electronic components. Evidently, the fabrication and integration to attain any monolithic micro-system may become difficult for complex multi-component structures and challenging when trying to incorporate non-traditional materials. Hence, these techniques may serve as fundamental guidelines and must be engineered into step-wise fabrication lines in order to obtain monolithically integrated micro-systems.

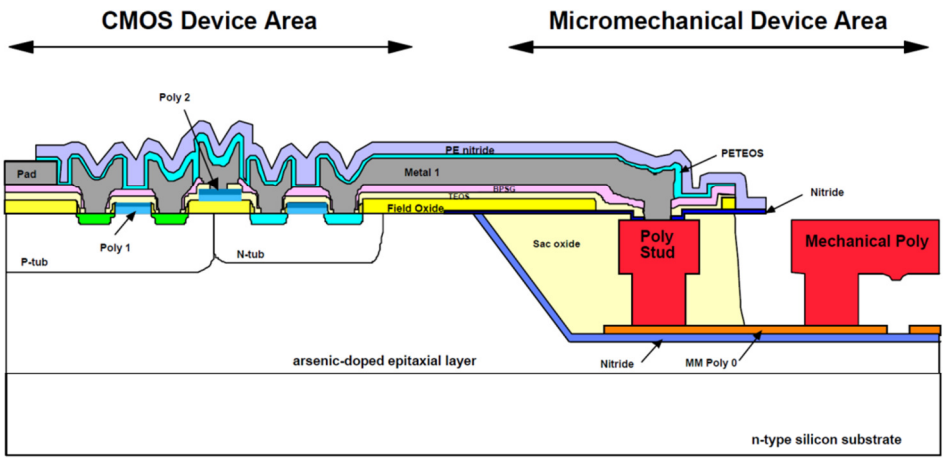

Figure 2.3. Schematic representation of the micromechanics-first approach to integration. In this example, micromechanical devices are fabricated in trenches etched in silicon wafers. The trenches are then refilled with oxide, planarized by chemical-mechanical polishing, annealed, and sealed. These wafers then form the starting material for a conventional microelectronic fabrication process. This approach may also have advantages in packaging of finished devices. Image courtesy of Sandia National Laboratories

Remarks:

- To achieve parallel integration of the micro-fuel cell along with other components and controlling electronics on the same chip, the fabrication line must be IC-compatible (*i.e.,* CMOS-compatible).
- Monolithically integrated micro-fuel cells are essentially a single layer-by-layer structure created on a single side of a substrate via MEMS / IC-compatible processes.
- To the best of our knowledge, monolithic μDLFCs have not yet been reported in literature mainly due to integration difficulties associated with the proton exchange membrane (Section 2.3.4).

2.3.3 Integration of the Proton Conductor

The central part of a fuel cell is the proton exchange membrane. The purpose of the proton exchange membrane is twofold: (1) to transport the protons from anode to cathode and (2) to serve as an effective separation barrier to avoid fuel and oxidant from mixing. Perfluorosulfonic acid polymer membranes (*e.g.,* Nafion from DuPont) are employed in the majority of μFC designs due to their high conductivity. However, Nafion membrane experiences significant volumetric fluctuations upon humidity variations which preclude viable integration [25]. Furthermore, the Nafion polymer (in solid or liquid form) is not photosensitive and cannot be resolved into high resolution patterns via photolithography. Nevertheless, Motokawa *et al.* reported a planar, monolithic μDLFC in which the membrane (Nafion) was fixed by mechanical compression [12]. Such a bulk integration of the proton exchange membrane not only prevents monolithic integration of the overall system (including the membrane) but causes a cross-talk effect when planar μFCs are connected in series to obtain higher power outputs [11]. To resolve the integration difficulties associated with the proton exchange membrane and to achieve a monolithic system, novel MEMS / IC-compatible proton exchange membranes with fine-line resolution capability and high conductivity must be developed.

Remarks:

- To achieve the monolithic integration of the overall microsystem (*i.e.,* μFC) and hence its parallel integration with other components and controlling electronics on the same chip, MEMS/ IC-compatible proton exchange membranes with fine-line resolution and high conductivity must be developed.

- To the author's knowledge, a MEMS / IC-compatible (*i.e.,* CMOS-compatible) proton exchange membrane has not yet been developed.
- Another feasible path to monolithic integration of micro-fuel cells is the omission of the proton exchange membrane as discussed in Section 1.2.2.

2.4 Thesis Overview

Building on these principles, the focus of this thesis is twofold: to design, fabricate, characterize, and optimize a planar, monolithically integrated, μLFFC suitable as an on-chip power source for 1-100 mW class applications **(Chapter 3)**, and to develop a fully couple three dimensional numerical model that includes all transport processes and electrochemical events that occur within an operating cell structure to gain qualitative and quantitative insight, and determine crucial design and operating parameters in the performance of LFFCs **(Chapter 4)**.

2.5 References

[1] Kennedy, B. March 4, 2009, "Portable power: Micro fuel cells provide power on the go", Available: http://www.micromanufacturing.com, Last accessed August 10, 2010.

[2] Nguyen, N. & Chan, S.H. 2006, "Micromachined polymer electrolyte membrane and direct methanol fuel cells - A review", *Journal of Micromechanics and Microengineering,* vol. 16, no. 4, pp. R1-R12.

[3] Yu, X. & Pickup, P.G. 2008, "Recent advances in direct formic acid fuel cells (DFAFC)", *Journal of Power Sources,* vol. 182, no. 1, pp. 124-132.

[4] Kjeang, E., Djilali, N. & Sinton, D. 2009, "Microfluidic fuel cells: A review", *Journal of Power Sources,* vol. 186, no. 2, pp. 353-369.

[5] Frank, M., Erdler, G., Frerichs, H.-., Müller, C. & Reinecke, H. 2008, "Chip integrated fuel cell accumulator", *Journal of Power Sources,* vol. 181, no. 2, pp. 371-377.

[6] Moore, C.W., Li, J. & Kohl, P.A. 2005, "Microfabricated fuel cells with thin-film silicon dioxide proton exchange membranes", *Journal of the Electrochemical Society,* vol. 152, no. 8, pp. A1606-A1612.

[7] Yamazaki, Y. 2004, "Application of MEMS technology to micro fuel cells", *Electrochimica Acta,* vol. 50, no. 2-3 SPEC. ISS., pp. 663-666.

[8] Kelley, S.C., Deluga, G.A. & Smyrl, W.H. 2002, "Miniature fuel cells fabricated on silicon substrates", *AICHE Journal,* vol. 48, no. 5, pp. 1071-1082.

[9] Ferrigno, R., Stroock, A.D., Clark, T.D., Mayer, M. & Whitesides, G.M. 2002, "Membraneless vanadium redox fuel cell using laminar flow", *Journal of the American Chemical Society,* vol. 124, no. 44, pp. 12930-12931.

[10] Choban, E.R., Markoski, L.J., Stoltzfus, J., Moore, J.S. & Kenis, P.J.A. 2002, "Microfluidic Fuel Cells that Lack a PEM", *Power Sources Proceedings*, vol. 40, 317-320.

[11] Xiao, Z., Feng, C., Chan, P.C.H. & Hsing, I.-. 2008, "Monolithically integrated planar microfuel cell arrays", *Sensors and Actuators, B: Chemical,* vol. 132, no. 2, pp. 576-586.

[12] Motokawa, S., Mohamedi, M., Momma, T., Shoji, S. & Osaka, T. 2004, "MEMS-based design and fabrication of a new concept micro direct methanol fuel cell (μ-DMFC)", *Electrochemistry Communications,* vol. 6, no. 6, pp. 562-565.

[13] Lee, S.J., Chang-Chien, A., Cha, S.W., O'Hayre, R., Park, Y.I., Saito, Y. & Prinz, F.B. 2002, "Design and fabrication of a micro fuel cell array with "flip-flop" interconnection", *Journal of Power Sources,* vol. 112, no. 2, pp. 410-418.

[14] Min, K., Tanaka, S. & Esashi, M. 2006, "Fabrication of novel MEMS-based polymer electrolyte fuel cell architectures with catalytic electrodes supported on porous SiO2", *Journal of Micromechanics and Microengineering,* vol. 16, no. 3, pp. 505-511.

[15] Tominaka, S., Ohta, S., Obata, H., Momma, T. & Osaka, T. 2008, "On-chip fuel cell: Micro direct methanol fuel cell of an air-breathing, membraneless, and monolithic design", *Journal of the American Chemical Society,* vol. 130, no. 32, pp. 10456-10457.

[16] Shen, M., Walter, S. & Gijs, M.A.M. 2009, "Monolithic micro-direct methanol fuel cell in polydimethylsiloxane with microfluidic channel-integrated Nafion strip", *Journal of Power Sources,* vol. 193, no. 2, pp. 761-765.

[17] López-Montesinos, P.O., Yossakda, N., Pelton, W. & Kenis, P.J.A. 2008, "Fabricación de una micropila de combustible de ácido fórmico directo (μ-DFAFC) de arquitectura plana: Vía a la integración monolítica", *Proceedings of III Congreso Nacional de Pilas de Combustible CONNAPICE*, pp. 437-440.

[18] Kundu, A., Jang, J.H., Gil, J.H., Jung, C.R., Lee, H.R., Kim, S., Ku, B. & Oh, Y.S. 2007, "Micro-fuel cells-Current development and applications", *Journal of Power Sources,* vol. 170, no. 1, pp. 67-78.

[19] Maynard, H.L. & Meyers, J.P. 2002, "Miniature fuel cells for portable power: Design considerations and challenges", *Journal of Vacuum Science and Technology B: Microelectronics and Nanometer Structures,* vol. 20, no. 4, pp. 1287-1297.

[20] Meyers, J.P. & Maynard, H.L. 2002, "Design considerations for miniaturized PEM fuel cells", *Journal of Power Sources,* vol. 109, no. 1, pp. 76-88.

[21] Yeom, J., Jayashree, R.S., Rastogi, C., Shannon, M.A. & Kenis, P.J.A. 2006, "Passive direct formic acid microfabricated fuel cells", *Journal of Power Sources,* vol. 160, no. 2 SPEC. ISS., pp. 1058-1064.

[22] Jayashree, R.S., Spendelow, J.S., Yeom, J., Rastogi, C., Shannon, M.A. & Kenis, P.J.A. 2005, "Characterization and application of electrodeposited Pt, Pt/Pd, and Pd catalyst structures for direct formic acid micro fuel cells", *Electrochimica Acta,* vol. 50, no. 24, pp. 4674-4682.

[23] Feng, C., Xiao, Z., Chan, P.C.H. & Hsing, I.-. 2006, "Lithography-free silicon micro-pillars as catalyst supports for microfabricated fuel cell applications", *Electrochemistry Communications,* vol. 8, no. 8, pp. 1235-1238.

[24] Smith, J.H., Montague, S. & Sniegowski, J.J. 1995, "Material and processing issues for the monolithic integration of microelectronics with surface-micromachined polysilicon sensors and actuators", *Proceedings of SPIE - The International Society for Optical Engineering*, pp. 64-73.

[25] Gold, S., Chu, K.-., Lu, C., Shannon, M.A. & Masel, R.I. 2004, "Acid loaded porous silicon as a proton exchange membrane for micro-fuel cells", *Journal of Power Sources,* vol. 135, no. 1-2, pp. 198-203.

[26] Bazylak, A., Sinton, D. & Djilali, N. 2005, "Improved fuel utilization in microfluidic fuel cells: A computational study", *Journal of Power Sources,* vol. 143, no. 1-2, pp. 57-66.

[27] Chang, M.-H., Chen, F. & Fang, N.-. 2006, "Analysis of membraneless fuel cell using laminar flow in a Y-shaped microchannel", *Journal of Power Sources,* vol. 159, no. 2, pp. 810-816.

[28] Choban, E.R., Markoski, L.J., Wieckowski, A. & Kenis, P.J.A. 2004, "Microfluidic fuel cell based on laminar flow", *Journal of Power Sources,* vol. 128, no. 1, pp. 54-60.

[29] López-Montesinos, P.O., Yossakda, N., Schmidt, A., Brushett, F.R., Pelton, W.E. & Kenis, P.J.A. 2011, "Design, fabrication, and characterization of a planar, silicon-based, monolithically integrated micro laminar flow fuel cell with a bridge-shaped microchannel cross-section", *Journal of Power Sources,* vol. 196, no. 10, pp. 4638-4645.

[30] Warneke, B.A. & Pister, K.S.J. 2002, "Exploring the limits of system integration with smart dust", *Proceedings of ASME International Mechanical Engineering Congress and Exposition*, pp. 621-625.

Chapter 3

Design, Fabrication, and Characterization of a Planar, Silicon-Based, Monolithically Integrated Micro Laminar Flow Fuel Cell

In this chapter, we describe the fabrication of a planar, silicon-based, monolithically integrated micro laminar flow fuel cell (μLFFC) using standard MEMS and IC-compatible fabrication technologies. The μLFFC operates with acid supported solutions of formic acid and potassium permanganate, as a fuel and oxidant, respectively. The micro-fuel cell design features two *in-plane* anodic and cathodic microchannels connected via a bridge to confine the diffusive liquid-liquid interface away from the electrode areas and to minimize crossover. Palladium high-active-surface-area catalyst was selectively integrated into the anodic microchannel by electrodeposition, whereas no catalyst was required in the cathodic microchannel. A three-dimensional (3D) diffusion-convection model was developed to study the behavior of the diffusion zone and to extract appropriate cell-design parameters and operating conditions. Experimentally, we observed peak power densities as high as 26 mW cm^{-2} when operating single cells at a flow rate of 60 μL min^{-1} at room temperature. The miniature membraneless fuel cell design presented herein offers potential for on-chip power generation, which has long been prohibited by integration complexities associated with the membrane.

---

* Part of this work has been published: López-Montesinos, P.O., Yossakda, N., Schmidt, A., Brushett, F.R., Pelton, W.E. & Kenis, P.J.A. 2011, "Design, fabrication, and characterization of a planar, silicon-based, monolithically integrated micro laminar flow fuel cell with a bridge-shaped microchannel cross-section", *Journal of Power Sources,* vol. 196, no. 10, pp. 4638-4645.

3.1 Introduction

Small, portable consumer electronics such as mobile phones, laptop computers, personal digital assistants, and global-positioning systems, have recently merged into single platforms and gained superior multitasking abilities in part enabled by major advances in wireless communication and data transmission [1]. The high resolution capability, batch production, and reproducibility accessible via microfabrication technologies for integrated circuits (IC) and microelectromechanical systems (MEMS) enable further miniaturization and integrated-device sophistication in a cost-effective manner [2-3]. Moreover, the next generation of MEMS, *i.e.,* sensors, actuators, and lab-on-a-chip devices, are expected to operate remotely to accomplish particular machine-enhanced human endeavors in the diverse arenas of medicine, environmental sciences, and engineering [4-6]. Miniaturized secondary (rechargeable) batteries such as Ni-Cd, Li-ion, and Li-polymer, while presently powering the vast majority of portable devices, may no longer feature the necessary energy density to cope with these new power demands and required device autonomy [7]. As an alternative, MEMS-based electrochemical energy converters such as micro-fuel cells (μFCs), particularly intended to operate with easily handled and stored liquid fuels (*e.g.,* methanol, formic acid), are envisioned as a possible solution due to their high energy density, efficiency, and quasi-instant recharge capability by easy reactant refilling [8-10].

Silicon-based μFCs offer the possibility of parallel integration with other electronic components on the same chip [11]. On-chip integration requires a compact μFC architecture that can be fabricated using standard MEMS / IC-compatible (*i.e.,* CMOS-compatible) technologies [12]. After the first silicon-based miniature fuel cell was reported [3], numerous researchers have pursued the miniaturization of the traditional proton-exchange membrane fuel cell (PEMFC) bilayer design, composed of two bipolar substrates for the delivery of reactants and

current collection clamped to a membrane-electrode assembly (MEA) [7]. To complete this complex multicomponent structure, hybrid integration using non-standard fabrication techniques (*e.g.,* catalyst painting, hot pressing, hot rolling) is required [8]. As an alternative, Mayers and Maynard proposed a micro-fuel cell architecture with anodic and cathodic channels formed on a single silicon substrate [13]. The use of a single substrate facilitates monolithic integration in a layer-by-layer, build-etch sequence using MEMS / IC-compatible technologies. This planar miniature fuel-cell design was mathematically modeled and proved to be a less effective alternative to the bilayer (bipolar) architecture, primarily due to surface-area penalties [14]. However, IC-compatible electrodeposition techniques to integrate high-active-surface-area catalysts [15-16] and surface texturing methods [17] have recently been documented. For instance, Motokawa et al. [18] demonstrated single-cell performance of a MEMS-based micro-direct-methanol fuel cell (μDMFC) based on the aforementioned principles. Table 3.1 offers a literature review on the development of planar, monolithic μFCs for on-chip integration. Despite major advances in system integration with particular cell performance, on-chip implementation remains difficult. The majority of these μFCs employ perfluorosulfonic acid polymer membranes (*e.g.,* Nafion) whose integration via MEMS / IC-compatible techniques has been nearly impossible. This issue has long prohibited absolute monolithic integration of these Microsystems for on-chip power generation

An authentic concept that simplifies the micro-fuel cell architecture by omitting the proton exchange membrane (PEM), deserves particular attention [21-22]. Laminar flow (membraneless) fuel cells (LFFCs) utilize the typical laminar state of flows through micrometer-scale domains to sustain the separation of convergent coflowing streams along a single channel without significant convective mixing while still allowing proton transport [23]. The diffusion

along the interface is limited and, hence, crossover is minimized. Anode and cathode electrodes are typically positioned on the opposing channel walls. This microfluidic fuel-cell system significantly reduces ohmic losses associated with the membrane as well as hydration/dehydration cycles and cathode flooding (i.e., water management) [22-23]. Moreover, by excluding the PEM, the traditional μFC stack coalesces into a single substrate, enhancing the possibilities of absolute on-chip monolithic integration with fabrication sequences tailored from MEMS and IC techniques. Using this concept, Tominaka *et al*. proposed a membraneless fuel cell with a monolithic structure, in which two electrodes were formed on a single substrate [24]. However, performance limitations were attributed to a limited oxygen supply through its passive air-breathing system. As an alternative, the utilization of liquid oxidants such as hydrogen peroxide (H_2O_2) [25-26], nitric acid (HNO_3) [27], and potassium permanganate ($KMnO_4$) [23, 28-29] has been known to improve cathode kinetics and enable micro-fuel cells to perform at higher power densities than with air-based approaches. Furthermore, liquid oxidants enable μFCs to perform in intriguing anaerobic applications such as submarine, sub-terrestrial, and space missions [1].

In the succeeding sections we describe the fabrication of a planar, silicon-based monolithically integrated μLFFC, using standard MEMS and IC-compatible techniques. The μLFFC features a bridge-shaped microchannel cross-section to confine the diffusive liquid-liquid interface away from the electrode areas while minimizing crossover. The performance of this cell, operated with formic acid as the fuel and potassium permanganate as the oxidant, is presented.

Table 3.1. Summary of the performance of planar, monolithic, micro-fuel cells proposed for on-chip integration. Only single cell performance is presented, unless otherwise noted.

Reference	**Year**	**Reactant** fuel / oxidant	**Catalyst** anode / cathode	**Electrode area** (cm^2)	**OCP** (V)	**P_{max}** ($mW\ cm^{-2}$)	**Current density at P_{max}** ($mA\ cm^{-2}$)
Lee et al. [19]	2002	H_2 /O_2	Pt / Pt	5.0	~0.9	~18	~50
Motokawa et al. [18]	2004	2 M CH_3OH / O_2-sat.	Pt-Ru / Pt	0.018	0.4	0.78	3.6
Min et al. [20]	2006	H_2 / air	Pt / Pt	0.156	0.45	0.4	0.26
Xiao et al. [12]	2008	H_2 / O_2	Pt-Ru / Pt-Ru	-	1.8 [a]	10.5 [a]	-
Tominaka et al. [24]	2008	2 M CH_3OH / air	Pt-Ru / Pd-Co	0.024	0.5	1.4 [b]	8 [b]
Shen et al. [36]	2009	1 M CH_3OH / 0.01 M H_2O_2	Pt-Ru / Pt	0.048	0.46	3.0	11
This work		1 M HCOOH / 0.144 M $KMnO_4$	Pd / none	0.024	1.35	26	28

[a] Value corresponds to two serially connected cells (twin cell array)
[b] The authors reported the net power and current in μW and μA, respectively

3.2 Experimental

3.2.1 µLFFC Fabrication and Monolithic Integration

The µLFFC was created and integrated in parallel using a set of MEMS and IC standard fabrication processes. In general, the procedure consisted of three UV-photolithographic steps followed by the corresponding additive or subtractive processes, as schematically illustrated in Figure 3.1. In detail, a prime grade, *p*-type, ‹100›-oriented, double-sided polished silicon wafer (University Wafer) that is 100 mm in diameter with a resistivity of 1-10 Ω-cm (Figure 3.1(a)) was spin coated with a positive-tone photoresist (AZ 4620, Clariant Co.) and exposed via photolithography using a mask aligner (Electronic Vision 420), Figure 3.1(b). The pattern was developed in diluted AZ400K (Clariant Co.) solution (Figure 3.1(c)) and subsequently etched to 10 µm via inductively coupled plasma–deep reactive-ion etching (ICP-DRIE, Plasma-Therm SLR 770). The remaining photoresist was removed using resist stripper (AZ-400T, Clariant Co.), Figure 3.1(d). At the end of this fabrication sequence, a pattern composed of partially etched feedholes (1 mm in diameter) and microchannels (100 µm in width) along with a fully etched central bridging region (100 µm in width) was obtained. A 3D isometric projection of this substrate is shown in Figure 3.1(e). Similarly, to completely etch the feedholes and microchannels the advanced substrate was spin coated with AZ4620 photoresist and a second photolithographic exposure was executed using the aforementioned mask aligner (Figure 3.1(f)). The new pattern was revealed with diluted AZ400K developer solution (Figure 3.1(g)) and etched 40 µm (or 65 µm) deeper via ICP-DRIE. Residual photoresist was stripped off of the sample using AZ-400T solution (Figure 3.1(h)). In addition, to ensure overall electrical insulation, a 5,000-Å silicon dioxide film was thermally grown by consecutive dry and steam oxidation steps at 1,100 °C using a manual oxidation furnace (Lindbergh-Tempress 8500), see

Figure 3.1(i). At this intermediate stage the whole μLFFC structure composed of anodic and cathodic microchannels connected via a partially opened central bridge has been completed (Figure 3.1(i)). Finally, to integrate the current collectors, the structure was coated with a negative-tone dry-film photoresist (MX5030, DuPont) using a hot-roll laminator (Modulam 130, Think & Tinker, Ltd.) at 110 °C at a controlled feeding rate of 20.3 mm s^{-1}. A third photolithographic exposure was performed using a mask aligner (Figure 3.1(k)) and the substrate was developed in 1 wt.% anhydrous sodium carbonate solution (Na_2CO_3, Think & Tinker, Ltd.) to generate the current collection pattern (Figure 3.1(l)). A 200-nm gold layer was deposited via DC magnetron sputtering ($\sim 10^{-2}$ Torr of argon background pressure), preceded by deposition of a 40-nm chrome adhesion thin film (Figure 3.1(m)). These Cr/Au current collectors were formed by lifting off the remaining dry-film photoresist in a 1.5 wt.% sodium hydroxide solution (NaOH, Aldrich) (Figure 3.1(n)). The final monolithic μLFFC (single cell) is illustrated in Figure 3.1(o).

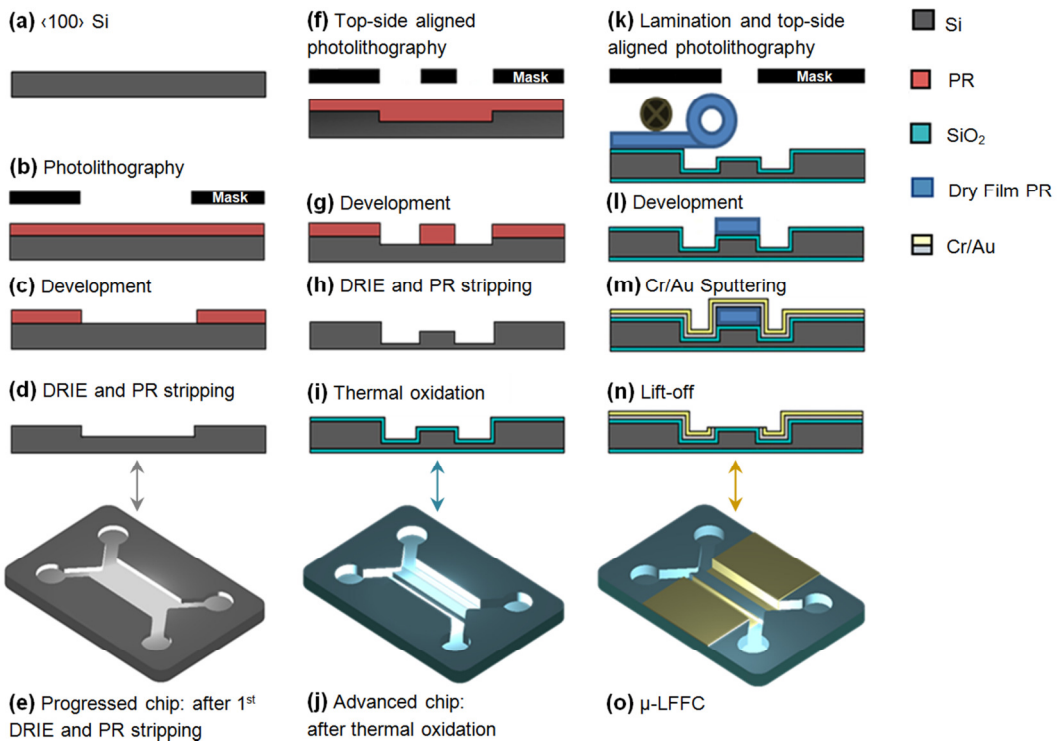

Figure 3.1. µLFFC fabrication flow scheme: (a)-(e) 10 µm DRIE, (f)-(j) 50 -75 µm DRIE (microchannels and feedholes) followed by Si thermal oxidation (SiO_2) and (k)-(o) integration of the Cr/Au current collectors.

3.2.2. IC-compatible Catalyst Deposition

A pure Pd high-active-surface-area catalyst layer was selectively integrated into the anodic microchannel of the μLFFC using a previously reported IC-compatible electrodeposition method [16]. The potentiostatic deposition was performed at −2 V versus Ag/AgCl reference electrode (BAS) in a 0.08 M $PdCl_2$ bath (5 wt.% in 10 wt.% HCl, Aldrich) for 45 s via a computer interfaced potentiostat/galvanostat (Autolab PGSTAT 30, Eco-Chemie). In addition, field-emission environmental scanning electron microscopy (ESEM-FEG, Philips XL30, FEI) was performed to confirm in-channel deposition and to assess morphological details. No catalyst was required in the cathodic microchannel.

3.2.3. μLFFC Assembly and Testing

An experimental microfluidic fixture (not a part of the monolithic design) was created for each fabricated μLFFC (Figure 3.2). In brief, poly(methyl methacrylate) (PMMA) top and basal substrates along with polydimethylsiloxane (PDMS) sealing and conformal layers were aligned to mechanically secured the μLFFC using nylon screws. Conductive copper adhesive films (Compac/TriMas) were used to contact the Cr/Au current collectors.

The performance of the μLFFCs was assessed at room temperature and atmospheric pressure using the aforementioned potentiostat/galvanostat. The μLFFCs were fed with 1 M HCOOH/0.5 M H_2SO_4 (Aldrich/GFS Chemicals Powell) and 144 or 60 mM $KMnO_4$/0.5 M H_2SO_4 (Fisher) as the fuel and the oxidant, respectively, using a syringe infusion pump (11 Plus, Harvard Apparatus). A 1:1 (fuel-to-oxidant) flow ratio was used with an input of 60 μL min^{-1}. Once the open-circuit potential (OCP) was determined, polarization curves were recorded by fixing the cell to a constant potential and reading the circuit current upon reaching steady-state conditions.

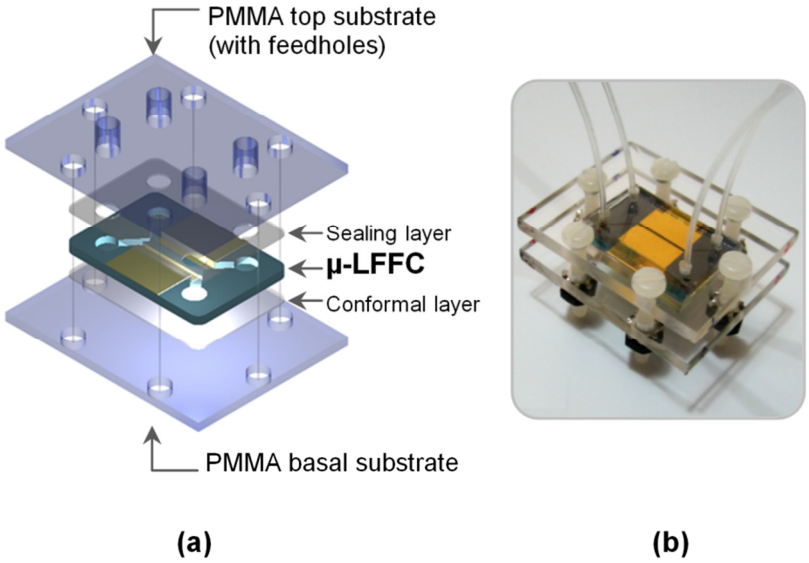

Figure 3.2. (a) Schematic layout of the μLFFC experimental microfluidic fixture (PMMA top and basal substrates, PDMS sealing and conformal layers aligned to mechanically seal the chip); (b) photograph of the μLFFC secured in its microfluidic fixture for performance tests. The chip footprint is 26 mm × 18 mm.

3.3 Results and Discussion

3.3.1 μLFFC Monolithic Integration

One of the strategies used to achieve the monolithic integration of the μLFFC is to minimize the number of process steps needed for fabrication. For instance, feedholes (1 mm in diameter, Figure 3.3(a), left) were created concurrently with the first and second DRIE processes designated to etch the central bridging region and microchannels, respectively. This approach eliminates the need for a double-sided alignment process and a separate DRIE step often required to incorporate traditional all-through feedholes. Figure 3.3(a) shows the μLFFC Y-shaped fluidic entry and microchannels connected via a central bridge where the fuel (1M HCOOH) and oxidant (60-144 mM $KMnO_4$) streams are permitted to interface.

Similarly, minimizing the number of layers without hindering fuel cell performance simplifies the fabrication line and promotes cost-effective monolithic integration. Figure 3.3(b)

shows the incorporation of pure Pd high-active-surface-area catalyst into the anodic microchannel of the μLFFC using the technique described in Section 3.2.2, whereas no catalyst was needed in the cathodic microchannel. The corrugated (left) and smooth (right) surfaces correspond to the integrated Pd catalytic layer and bare Cr/Au cathodic current collector, respectively. The choice of a self-activated cathodic electron acceptor such as MnO_4^- as an alternative to catalyst-dependent oxidants such as oxygen eliminates the need to integrate an electroactive material into the cathodic microchannel. Compared to the dual anode-to-cathode catalyst system (e.g., Pt-Ru / Pt) required in the majority of micro-fuel cell designs, the use of a single-anode catalyst system reduces the complexity of the steps required for precious-metal incorporation, which facilitates monolithic integration. Figure 3.3(c) offers a magnified view of the electrodeposited Pd catalyst, which consists of a variety of spherical entities of round crystallites and fibrous surfaces. Further information on its structural characterization, electrocatalytic analysis, and its use for formic acid oxidation is available elsewhere [16]. Figure 3.3(d) shows a cross-sectional view of the Pd catalyst-based anodic microchannel. SEM and profilometry (data not shown) suggested an average Pd catalyst-layer thickness of approximately 7 μm.

3.3.2. μLFFC Performance

The performance of two μLFFCs with bridge-shaped microchannel cross-sections (denoted Chip A and Chip B in this section) was assessed at room temperature and atmospheric pressure. For the geometric parameters corresponding to these chips, refer to Section 4.3 (Figure 4.1, page 50). Chip A and B only differ in microchannel depth (50 vs. 75, respectively). The chips have identical footprints (length × width) of 26 mm × 18 mm (see the photograph in Figure 3.2).

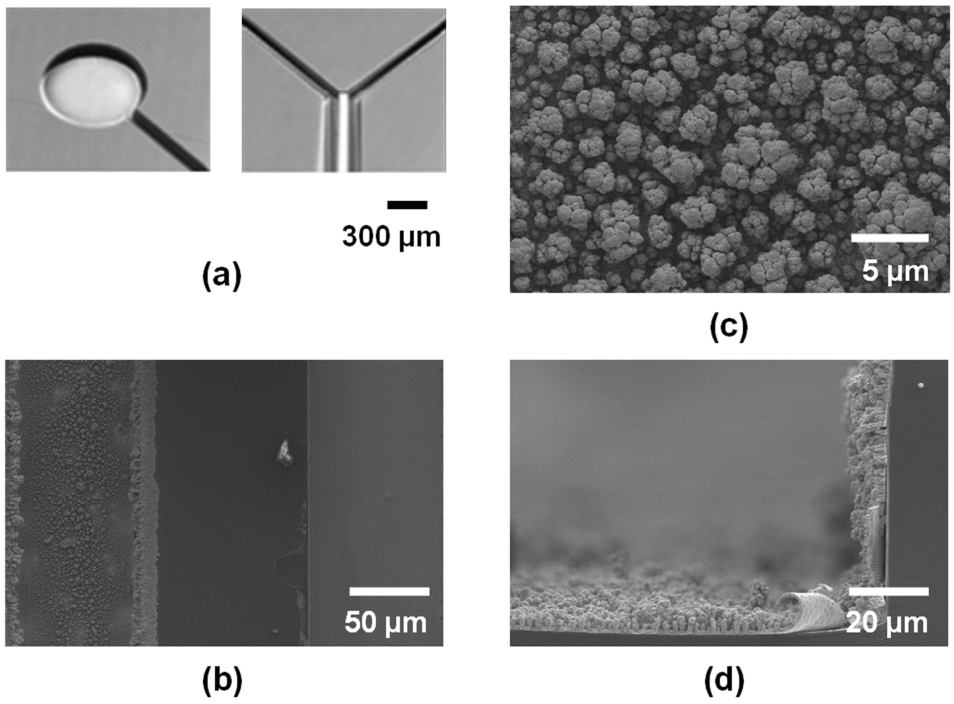

Figure 3.3. Alpha-Step IQ camera and ESEM micrographs: (a) feedholes (left micrograph) and Y-shaped fluidic entry and microchannels after the second DRIE process (right micrograph); (b) electrodeposited Pd on Cr/Au sputtered anodic microchannel (left channel) and Cr/Au bare cathodic channel (right channel, no catalyst); (c) electrodeposited Pd on Cr/Au anodic microchannel at higher magnification; and (d) cross-sectional view of the Pd catalyst-based anodic microchannel.

Chip A was operated with 1 M HCOOH / 0.5 M H_2SO_4 and variable oxidant concentrations of 60 mM and 144 mM $KMnO_4$ / 0.5 M H_2SO_4, each at a flow rate of 60 µL min^{-1}. The unitary fuel-to-oxidant flow ratio ensured positioning of the liquid-liquid interface near the midline along the bridge location. The polarization (open squares and circles) and power-density (filled squares and circles) curves of Chip A are shown in Figure 3.4(a). When the chip was operated at the low oxidant concentration of 60 mM $KMnO_4$, an open-circuit potential (OCP) of 1.4 V was attained. In addition, a maximum power density of 10.0 mW cm^{-2} was obtained at a cell voltage and current density of 0.6 V and 10.4 mA cm^{-2}, respectively. In contrast, when the same chip

was operated at the higher oxidant concentration of 144 mM $KMnO_4$, an OCP value of 1.34 V was achieved. Under these conditions, the chip delivered a peak power density of 19.2 mW cm^{-2} at a cell voltage and current density of 0.7 V and 27.4 mA cm^{-2}, respectively.

Similarly, Chip B was operated with 1 M HCOOH / 0.5 M H_2SO_4 and a fixed oxidant concentration of 144 mM $KMnO_4$ / 0.5 M H_2SO_4, each at a of flow rate of 60 µL min^{-1}. The polarization (open squares) and power-density (filled squares) curves of Chip B are shown in Figure 3.4(b). An OCP of 1.35 V was attained, nearly identical to the OCP measured for Chip A. The power density reached a peak value of 25.5 mW cm^{-2} at a cell voltage and current density of 0.9 V and 28.3 mA cm^{-2}, respectively.

The OCPs of formic acid (membraneless) LFFCs (of hybrid and monolithic integration) typically range from 0.6 V to 1.2 V for a variety of oxidants including potassium permanganate [23, 28-31]. The reported increase in OCP herein may be due not only to the high redox potential of permanganate in acidic conditions (E^0 = 1.70V) [32] but also to the minimal reactant crossover when employing a bridge-shaped microchannel configuration.

In practical applications, a fuel cell is operated at a certain operating point that does not necessarily correspond to the maximum power density. Instead it is operated at a nominal power output that is a good compromise between cell efficiency, low capital cost, and operational stability [33]. In general, high voltage improves efficiency and lowers fuel consumption [33]. The µLFFCs studied here can be operated at nominal power (typically 0.6 – 0.7 V, [33]) as well as at higher potentials, even exceeding 1V due to their high OCP values.

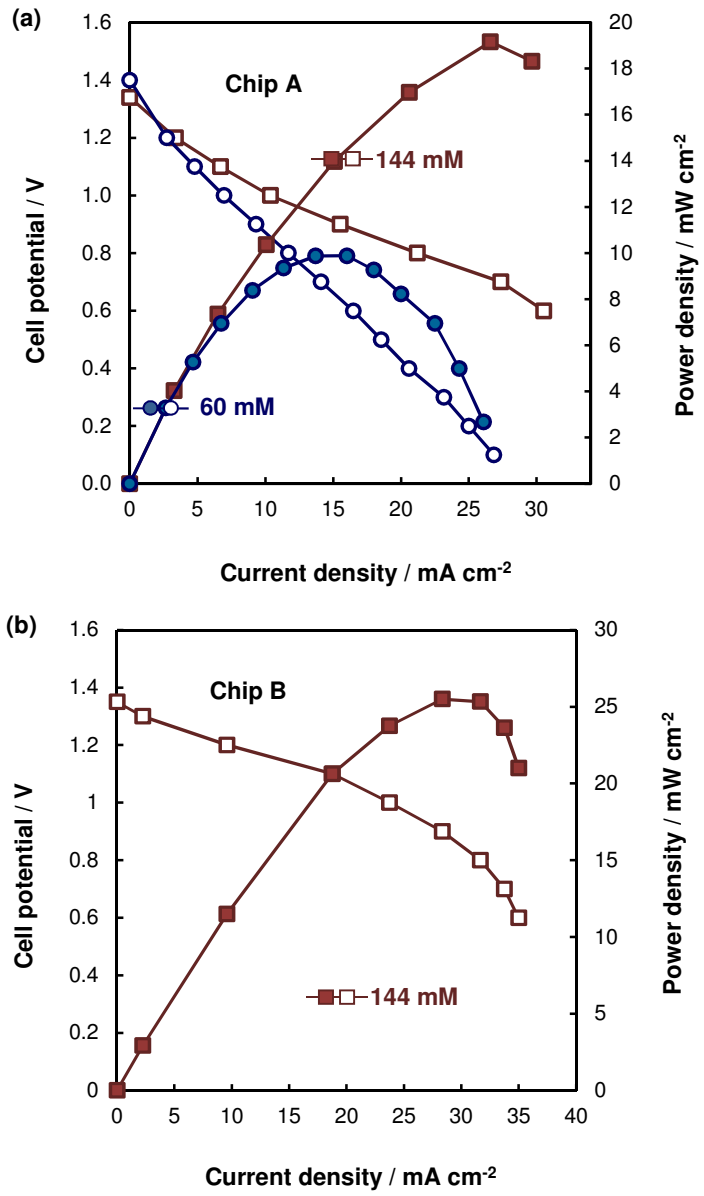

Figure 3.4. Polarization (open squares and circles) and power-density (filled squares and circles) curves for: (a) Chip A operating with 1 M HCOOH and two $KMnO_4$ concentrations (144 mM and 60 mM), all at flow rates of 60 µL min^{-1}; and (b) Chip B operating with 1 M HCOOH and 144 mM $KMnO_4$, each at a flow rate of 60 µL min^{-1}.

When operated under the same experimental conditions, Chip B exhibited a ~25% higher maximum power density than Chip A (Figure 3.4). Chip B has a deeper microchannel than Chip A (75 µm vs. 50 µm). The larger channel cross-sectional area of Chip B leads to a lower linear velocity at the inlet compared to Chip A (133 mm s^{-1} vs. 200 mm s^{-1}). As modeled by Bazylak *et*

al. [34], lowering inlet velocity in a low aspect-ratio rectangular channel geometry results in improved fuel utilization and superior performance due to an increase in reactant residence time. However, the extent to which velocity can be reduced depends upon maintaining a good compromise between fuel utilization, reduction of the depletion region [34-35] and the mixing zone.

According to the comprehensive review on planar, monolithic micro-fuel cells (Table 3.1), we have demonstrated improvement in cell performance. As noted from the peak power density values (P_{max}), our μLFFCs measured favorably. In particular, compared to a passive, membraneles, monolithic μFC with similar electrode area [24], our μLFFCs exhibited more than 2 orders of magnitude increase in power density. However, energy losses associated with active reactant delivery (*i.e.,* pumps) for systems with similar flow head resistance have been reported as ~100 μW [24]. This value remains in agreement with the pressure drops calculated for our cells (see Table A.1 in Appendix). Yet considering these ancillary losses, the power output of our cells remains significantly higher. The marked increase in power density may be attributed to synergistic effects. The use of pure Pd catalyst facilitates the '*direct electro-oxidation*' of formic acid at low temperatures. The direct pathway suppresses intermediate reaction steps that often lead to CO formation and subsequent catalyst poisoning [16]. Therefore, we expect enhanced anode activation and reaction kinetics at low temperatures. Similarly, improved cathode kinetics is expected by using potassium permanganate due to a much lower activation barrier for electron transfer compared to oxygen [1]. Furthermore, the cell bridge-shaped architecture and operating conditions had a positive impact on cell performance by further reducing crossover (i.e., preventing mixed potential) and enhancing reactant transport to the electrodes and their utilization.

3.4 Summary

We have fabricated a planar, silicon-based, monolithically integrated, μLFFC suitable as an on-chip power source. The MEMS-based, IC-compatible (*i.e.,* CMOS-compatible) fabrication line of these cells may facilitate their integration with other components and controlling electronics on the same chip. A new bridge-shaped microchannel cross-section was explored to reduce fuel-to-oxidant interfacial contact, thereby minimizing reactant crossover. A second rationale to employ this microchannel geometry was to separate the mixing and reaction zones over the entire flow domain to enhance reactant transport to the electrodes and improve fuel utilization. A 3-D diffusion-convection computational model was developed to examine the behavior of the mixing zone and extract cell-design parameters and operating conditions. For the μLFFCs presented herein, the model suggested reactant flow rates ranging from 50-60 μL min^{-1} to enable the confinement of the mixing zone along the bridge and avoid its interaction with the electrode areas during operation. Experimentally, we observed high OCP values (1.34-1.35 V) which is an indication of the minimum reactant crossover that occurs by employing a bridge-shaped microchannel cross-section. These OCP values are 13 % higher than those reported in literature for formic acid / potassium permanganate cells [23, 28-29]. The μLFFCs delivered peak power densities of 19 and 26 mW cm^{-2} when operated with 1 M HCOOH / 0.5 M H_2SO_4 and 144 mM $KMnO_4$ / 0.5 M H_2SO_4 as fuel and oxidant, respectively, at a flowrate of 60 μL min^{-1}. Further refinements to these methods should be pursued to optimize the proton aperture (*i.e.,* the bridge height) to minimize cell resistance. The proposed micro-fuel cell design: planar, membraneless, monolithic, and CMOS-compatible, may offer a solution to the next generation of MEMS and consumer electronics whose highly integrated platforms demand on-chip incorporation of the power source. On-chip integration of power sources fosters overall device

miniaturization, weight and cost reduction, batch production, and reproducibility desired for commercial interests.

3.5 References

[1] Morse, J.D. 2007, "Micro-fuel cell power sources", *International Journal of Energy Research,* vol. 31, no. 6-7, pp. 576-602.

[2] Yamazaki, Y. 2004, "Application of MEMS technology to micro fuel cells", *Electrochimica Acta,* vol. 50, no. 2-3 SPEC. ISS., pp. 663-666.

[3] Kelley, S.C., Deluga, G.A. & Smyrl, W.H. 2002, "Miniature fuel cells fabricated on silicon substrates", *AICHE Journal,* vol. 48, no. 5, pp. 1071-1082.

[4] La O', G.J., In, H.J., Crumlin, E., Barbastathis, G. & Shao-Horn, Y. 2007, "Recent advances in microdevices for electrochemical energy conversion and storage", *International Journal of Energy Research,* vol. 31, no. 6-7, pp. 548-575.

[5] Flipsen, S.F.J. 2006, "Power sources compared: The ultimate truth?", *Journal of Power Sources,* vol. 162, no. 2 SPEC. ISS., pp. 927-934.

[6] D. Dunn-Rankin, E.M. Leal, D.C. Walther, Personal power systems, Progress in Energy and Combustion Science 31 (2005) 422-465.

[7] Kundu, A., Jang, J.H., Gil, J.H., Jung, C.R., Lee, H.R., Kim, S., Ku, B. & Oh, Y.S. 2007, "Micro-fuel cells-Current development and applications", *Journal of Power Sources,* vol. 170, no. 1, pp. 67-78.

[8] Nguyen, N. & Chan, S.H. 2006, "Micromachined polymer electrolyte membrane and direct methanol fuel cells - A review", *Journal of Micromechanics and Microengineering,* vol. 16, no. 4, pp. R1-R12.

[9] Yu, X. & Pickup, P.G. 2008, "Recent advances in direct formic acid fuel cells (DFAFC)", *Journal of Power Sources,* vol. 182, no. 1, pp. 124-132.

[10] Kjeang, E., Djilali, N. & Sinton, D. 2009, "Microfluidic fuel cells: A review", *Journal of Power Sources,* vol. 186, no. 2, pp. 353-369.

[11] Frank, M., Erdler, G., Frerichs, H.-., Müller, C. & Reinecke, H. 2008, "Chip integrated fuel cell accumulator", *Journal of Power Sources,* vol. 181, no. 2, pp. 371-377.

[12] Xiao, Z., Feng, C., Chan, P.C.H. & Hsing, I.-. 2008, "Monolithically integrated planar microfuel cell arrays", *Sensors and Actuators, B: Chemical,* vol. 132, no. 2, pp. 576-586.

[13] Maynard, H.L. & Meyers, J.P. 2002, "Miniature fuel cells for portable power: Design considerations and challenges", *Journal of Vacuum Science and Technology B: Microelectronics and Nanometer Structures,* vol. 20, no. 4, pp. 1287-1297.

[14] Meyers, J.P. & Maynard, H.L. 2002, "Design considerations for miniaturized PEM fuel cells", *Journal of Power Sources,* vol. 109, no. 1, pp. 76-88.

[15] Yeom, J., Jayashree, R.S., Rastogi, C., Shannon, M.A. & Kenis, P.J.A. 2006, "Passive direct formic acid microfabricated fuel cells", *Journal of Power Sources,* vol. 160, no. 2 SPEC. ISS., pp. 1058-1064.

[16] Jayashree, R.S., Spendelow, J.S., Yeom, J., Rastogi, C., Shannon, M.A. & Kenis, P.J.A. 2005, "Characterization and application of electrodeposited Pt, Pt/Pd, and Pd catalyst structures for direct formic acid micro fuel cells", *Electrochimica Acta,* vol. 50, no. 24, pp. 4674-4682.

[17] Feng, C., Xiao, Z., Chan, P.C.H. & Hsing, I.-M. 2006, "Lithography-free silicon micro-pillars as catalyst supports for microfabricated fuel cell applications", *Electrochemistry Communications,* vol. 8, no. 8, pp. 1235-1238.

[18] Motokawa, S., Mohamedi, M., Momma, T., Shoji, S. & Osaka, T. 2004, "MEMS-based design and fabrication of a new concept micro direct methanol fuel cell (μ-DMFC)", *Electrochemistry Communications,* vol. 6, no. 6, pp. 562-565.

[19] Lee, S.J., Chang-Chien, A., Cha, S.W., O'Hayre, R., Park, Y.I., Saito, Y. & Prinz, F.B. 2002, "Design and fabrication of a micro fuel cell array with "flip-flop" interconnection", *Journal of Power Sources,* vol. 112, no. 2, pp. 410-418.

[20] Min, K., Tanaka, S. & Esashi, M. 2006, "Fabrication of novel MEMS-based polymer electrolyte fuel cell architectures with catalytic electrodes supported on porous SiO2", *Journal of Micromechanics and Microengineering,* vol. 16, no. 3, pp. 505-511.

[21] Ferrigno, R., Stroock, A.D., Clark, T.D., Mayer, M. & Whitesides, G.M. 2002, "Membraneless vanadium redox fuel cell using laminar flow", *Journal of the American Chemical Society,* vol. 124, no. 44, pp. 12930-12931.

[22] Choban, E.R., Markoski, L.J., Stoltzfus, J., Moore, J.S. & Kenis, P.J.A. 2002, "Microfluidic Fuel Cells that Lack a PEM", *Power Sources Proceedings*, vol. 40, 317-320.

[23] Choban, E.R., Markoski, L.J., Wieckowski, A. & Kenis, P.J.A. 2004, "Microfluidic fuel cell based on laminar flow", *Journal of Power Sources,* vol. 128, no. 1, pp. 54-60.

[24] Tominaka, S., Ohta, S., Obata, H., Momma, T. & Osaka, T. 2008, "On-chip fuel cell: Micro direct methanol fuel cell of an air-breathing, membraneless, and monolithic design", *Journal of the American Chemical Society,* vol. 130, no. 32, pp. 10456-10457.

[25] Miley, G., Luo, N., Mather, J., Byrd, E., Burton, R., Hawkins, G., Gimlin, R., Kopec, G., Shrestha, P., Benavides, G., Laystrom, J., Rusek, J., Valdez, T. & Narayanan, S. 2006, "Compact high-power-density direct NaBH4/H2O2 fuel cells", *8th Annual International*

Symposium Small Fuel Cells; Small Fuel Cells for Portable Applications, Washington DC.

[26] Valdez, T.I. & Narayanan, S.R. 2001, "Hydrogen peroxide oxidant fuel cell systems for ultra-portable applications", *Proceedings of the Electrochemical Society*, Pennington, NJ, pp. 265-273.

[27] Homa, A. 2005, "Alternative approaches for DMFC design: Silicon-based systems", *7th Annual International Symposium Small Fuel Cells*, Washington, DC.

[28] Sun, M.H., Velve-Casquillas, G., Guo, S.S., Shi, J., Ji, H., Ouyang, Q. & Chen, Y. 2007, "Characterization of microfluidic fuel cell based on multiple laminar flow", *Microelectronic Engineering,* vol. 84, no. 5-8, pp. 1182-1185.

[29] Salloum, K.S., Hayes, J.R., Friesen, C.A. & Posner, J.D. 2008, "Sequential flow membraneless microfluidic fuel cell with porous electrodes", *Journal of Power Sources,* vol. 180, no. 1, pp. 243-252.

[30] Jayashree, R.S., Gancs, L., Choban, E.R., Primak, A., Natarajan, D., Markoski, L.J. & Kenis, P.J.A. 2005, "Air-breathing laminar low-based microfluidic fuel cell", *Journal of the American Chemical Society,* vol. 127, no. 48, pp. 16758-16759.

[31] Cohen, J.L., Westly, D.A., Pechenik, A. & Abruña, H.D. 2005, "Fabrication and preliminary testing of a planar membraneless microchannel fuel cell", *Journal of Power Sources,* vol. 139, no. 1-2, pp. 96-105.

[32] Li, J., Fu, Q., Liao, Q., Zhu, X., Ye, D.-. & Tian, X. 2009, "Persulfate: A self-activated cathodic electron acceptor for microbial fuel cells", *Journal of Power Sources,* vol. 194, no. 1, pp. 269-274.

[33] Barbir, F. 2005, *PEM Fuel Cells - Theory and Practice*, Elsevier Academic Press.

[34] Bazylak, A., Sinton, D. & Djilali, N. 2005, "Improved fuel utilization in microfluidic fuel cells: A computational study", *Journal of Power Sources,* vol. 143, no. 1-2, pp. 57-66.

[35] Chang, M.-H., Chen, F. & Fang, N.-. 2006, "Analysis of membraneless fuel cell using laminar flow in a Y-shaped microchannel", *Journal of Power Sources,* vol. 159, no. 2, pp. 810-816.

[36] Shen, M., Walter, S. & Gijs, M.A.M. 2009, "Monolithic micro-direct methanol fuel cell in polydimethylsiloxane with microfluidic channel-integrated Nafion strip", *Journal of Power Sources,* vol. 193, no. 2, pp. 761-765.

Chapter 4

A Three-Dimensional Numerical Model of a Micro Laminar Flow Fuel Cell with a Bridge-shaped Microchannel Cross-section

Experimental characterization methods combined with mathematical modeling reduce the cost and time for building superior micro-fuel cells. The principles of a working micro-fuel cell are of strongly coupled, non-linear multiphysics nature. Therefore, the change of one operating parameter (*e.g.,* reactant concentration, flow rate) may induce a chain of physicochemical and electrochemical events that produces a non-obvious impact in overall micro-fuel cell integrity, performance, and efficiency. Therefore, developing a fully-coupled numerical model that includes all transport processes and electrochemical phenomena that occur within an operating micro-fuel cell may help in its design, characterization, and optimization. In general, these models often require the use of mass, momentum, species, and charge balances along with Butler-Volmer equations for electrode kinetics to obtain reasonable results [1-2]. The validation of a numerical model often requires experimental confirmation. Nevertheless, once the numerical solutions are in close agreement with experimental data, the model becomes a virtual tool for performance predictions, optimization, and step-wise design of superior micro-fuel cells. In this chapter we present a three-dimensional (3D) numerical model of a new micro laminar flow fuel cell with a bridge-shaped microchannel cross-section recently reported in literature by the present author [3]. The foremost goal here is to reveal all possible physicochemical and electrochemical phenomena that occur within the operating micro-fuel cell to study their impact on overall cell performance. Also, studies on reactants utilization, reactants crossover, and ancillary power losses (*i.e.,* active cell design) will be highlighted and discussed.

4.1. Introduction

Recently, there is a notable interest in developing ***on-chip*** integrated micro-fuel cells as new power sources for portable technologies and lab-on-a-chip devices with extremely small form factor (*e.g.,* biomedical micro-devices, micro-vehicles, micro-robots) [4-9]. The possibility of co-fabricating a power source along with other electronic components on the same chip enables overall device miniaturization, weight and cost reduction, and improved signal integrity with a minimum number of interconnects [10-11]. Laminar flow fuel cells (LFFCs), which significantly simplify micro-fuel cell architecture by omitting the proton exchange membrane (PEM), have motivated researchers to go from purely miniaturization efforts to ***on-chip*** integration [3,8]. By excluding the proton exchange membrane, the traditional micro-fuel cell stack (*i.e.,* bipolar plates, membrane electrode assembly) coalesces into a single substrate, enhancing the possibility of full ***on-chip*** monolithic integration with fabrication sequences tailored from MEMS and IC techniques [3,8].

LFFCs utilize the characteristic laminar state of flows at the microscale to sustain the separation of coflowing fuel and oxidant streams in a single channel [13]. The diffusion along the interface is limited and, hence, fuel crossover is minimized while proton transport can still occur. The anode and cathode electrodes are typically positioned on opposing channel walls. This micro-fuel cell configuration significantly reduces ohmic losses associated with the membrane as well as hydration/dehydration cycles and cathode flooding (*i.e.,* water management) [12, 13]. Using this concept, Tominaka *et al*. proposed a membraneless fuel cell with a monolithic structure, in which two electrodes were formed on a single substrate [8]. However, performance limitations were attributed to a limited oxygen supply through its passive air breathing system.

Recently, we have demonstrated that LLFCs can be successfully miniaturized and monolithically integrated via MEMS/IC batch fabrication techniques [3]. In brief, we have reported an on-chip integrated μLFFC that utilizes liquid oxidant (*i.e.,* potassium permanganate) to improve cathode kinetics and produce higher power outputs [3]. In succeeding sections we present a three dimensional numerical model to study the effect of all evolving physicochemical and electrochemical phenomena within an operating micro-fuel cell on its overall performance. Accordingly, new cell designs and operating parameters will be proposed and discussed. Indeed, the micro-fuel cell model presented herein may serve as a virtual tool for theoretical characterization and optimization of LFFCs.

4.2 The Importance of Channel Geometry in LFFCs

In typical LFFCs, anode and cathode catalyst-based electrodes are integrated on the opposite walls of a single rectangular channel. The design of a single flow field and the exclusion of a PEM are possible when streams coflow in the laminar state, self-constrained to their respective electrodes, while protons are able to migrate from anode to cathode. The only "separator" between the fuel and oxidant streams is essentially a liquid-liquid interface. Because the miscibility of the fuel and oxidant of choice is typically high, the liquid-liquid interface evolves into a diffusion (or mixing) zone which gradually increases in width as flow advances to the exit. Therefore, fuel crossover may occur and cell performance degrades. In such a scenario, strategic adjustments to the geometry of the main channel and upstream flow conditions allow for control over the width of the diffusion zone and the extent of crossover [1-2]. The width of the mixing zone can be predicted from the results of the scaling analysis [14]

$$\Delta x \approx \left(\frac{DHy}{U_y}\right)^{\frac{1}{3}} \tag{4.1}$$

where D is the diffusivity of the species, H is the height of the channel, U_y is the average flow velocity, and y the distance the fluid flows downstream. Bazylak *et al*. simulated the effects of geometric variations to the main channel and determined that a higher aspect ratio (width:height) result in a thinner diffusive interface and improved fuel utilization [1]. Later, Chang *et al*. correlated improvements in cell performance to the degree of mixing as characterized by the Péclet number ($Pe = U_yH/D$) [2]. In their study, the diffusion transverse to the direction of flow (fuel crossover) was minimized by increasing the aspect ratio of the main channel, which involves a reduction in channel height (H). Consequently, both the average velocity and the Péclet number increase. Because increasing the aspect ratio minimizes the mixing width and crossover but also sacrifices electrode area, variations to the conventional rectangular channel geometry merit further exploration [15-16]. In this chapter we present a three dimensional numerical model of an on-chip integrated micro-fuel cell recently reported in literature by the present author [3]. First, a simplified version of the model is presented in Section 4.4 where electrochemical reactions are excluded from the system. This first part of the model enabled us to inspect the behavior of the mixing zone and quantify fuel crossover upon geometrical adjustments to the main channel and upstream flow conditions (*i.e.,* reactant flow rate, reactant concentration). Second, a complete model that couples all transport processes and electrochemical phenomena that occur within a working μLFFC will be presented in Section 4.5.

4.3 Geometry Definition

The main objective of the bridge-shaped microchannel geometry of our micro laminar flow fuel cell is to minimize fuel-to-oxidant diffusive contact and isolate the corresponding mixing zone from the electrode areas while enabling efficient proton transport [3]. A bridge-shaped

microchannel cross-section provides more walls for electrode integration, thus increasing the reactive area. This configuration enables anode and cathode electrochemical reactions to proceed more efficiently as minimal or no interaction between the mixing region and the reaction zones is observed. Figure 4.1 illustrates top and cross-sectional views of the microchannel structure along with its geometric parameters. In our analysis 3 geometries were modeled (AR 10, AR 5, and AR 4) classified according to their bridge aspect ratio (AR). AR is defined here as the ratio of the bridge width to the bridge height (X in Figure 4.1), where X is variable and takes values of 10 μm, 20 μm, and 25 μm for AR = 10, AR = 5, and AR = 4, respectively. The three geometries were examined via numerical modeling.

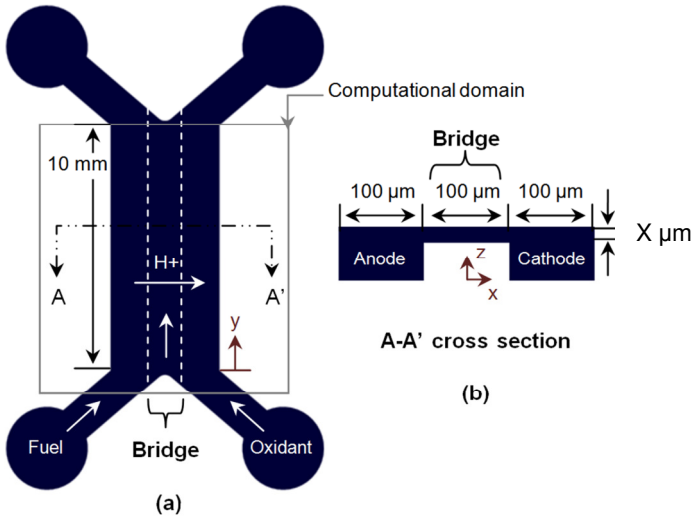

Figure 4.1. Schematic illustration of the bridge-shaped microchannel structure and geometrical parameters used in the simulations (X is variable): (a) top view; (b) cross-sectional view.

4.4 Mixing-zone Model

To predict the behavior of the diffusion zone, quantify fuel crossover, and assess appropriate cell-design parameters and operating conditions, a three-dimensional model was developed using the commercial finite-element-method (FEM) software COMSOL Multiphysics 3.4 (COMSOL,

Stockholm, Sweden). As illustrated in Figure 4.1(a), fuel (formic acid) and oxidant (potassium permanganate) streams enter separately through a Y-shaped entry, merge at the bridge location, and flow in parallel towards the exit. The computational domain consists of two sub-domains, namely, the anodic and cathodic flow channels. This allowed us to assign different physical properties and input conditions for each stream. For this simplified version of the model, the subdomains corresponding to the catalyst layers and current collectors are not included. Instead they are included in the complete fuel cell model discussed in Section 4.5. Physical properties and input parameters used in this first part of the simulations are included in Appendix A.

4.4.1 Assumptions

The following assumptions were made to obtain simplified versions of the governing equations:

(i) the density of the fluids (ρ) is constant,

(ii) the fluids are Newtonian with constant viscosity (μ),

(iii) the flow field is steady,

(iv) the system experiences negligible body forces,

(v) the cell operation is isothermal,

(vi) the mixing zone develops at a distant location from the electrode surface areas, so electrochemical reactions (depletion regions) have minimal impact on the local concentration gradient in the mixing zone, especially at low current densities.

4.4.2 Governing Equations

Using assumption (i), the general form of the mass-balance (continuity) equation for rectangular coordinates becomes:

$$\nabla \cdot \mathbf{u} = 0 \tag{4.2}$$

where **u** is the velocity vector. Similarly, by applying assumptions (i) and (ii), a special case of the momentum-balance equation (Navier-Stokes) is obtained:

$$\rho\,(\partial \mathbf{u}/\,\partial t \;+\; u\,.\nabla \mathbf{u}\,) = -\nabla p \;+ \mu \nabla^2\,\mathbf{u} + \rho \mathbf{b} \tag{4.3}$$

p denotes pressure and **b** is the body-force vector. Further, utilizing assumptions (iii) and (iv), the Navier-Stokes equation reduces to:

$$\rho\,(\mathbf{u}\,.\nabla \mathbf{u}\,) = -\nabla p \;+ \mu \nabla^2 \mathbf{u}\,. \tag{4.4}$$

Finally, under assumption (vi), the transport of species is of pure convective-diffusive nature and can be described by:

$$\nabla\,.\,(-D\nabla c \;+\; c\mathbf{u}) \;=\; 0 \tag{4.5}$$

where c is the concentration of a species and D indicates the corresponding diffusivity. Equations (4.2), (4.4) and (4.5) are coupled and simultaneously solved by applying system boundary conditions to obtain velocity and concentration fields.

4.4.3 Boundary Conditions

The velocity solution is obtained by applying the following boundary conditions to Equations (4.2) and (4.4),

$p = p_{in}$, $p_{in} = \Delta p_{cell}$; inlets (4.6)

$p = 0$; outlets (4.7)

when a zero-pressure condition is applied to the outlet, the inlet pressure (p_{in}) represents the cell pressure drop (Δp_{cell}). The no-slip condition is applied to all channel walls:

$\mathbf{u} = 0$; walls. (4.8)

Next, the velocity solution is coupled with Equation (4.5) and the following boundary conditions apply:

$c = c_{in}$; inlets (4.9)

where c_{in} is defined as the inlet concentration for the species of interest. A convective-flux condition is imposed to the outlet boundaries:

$\mathbf{n} \cdot (-D\nabla c) = 0$; outlets (4.10)

while no mass transport can take place through walls:

$\mathbf{n} \cdot (-D\nabla c + c\mathbf{u}) = 0$; walls. (4.11)

4.4.4 Fuel Crossover Quantification

The fuel crossover quantification (mol s^{-1}) was performed in COMSOL Multiphysics by including a boundary that is solely used to evaluate mass transport over it (Figure 4.2). Since this boundary is not necessary to solve the model, it can be set to "continuity" when boundary conditions are established. However, after the model has been solved, the boundary can be used in the post-processing tasks to quantify how much fuel has crossed to the cathodic micro flow channel. The appropriate way to do this in COMSOL is by performing boundary integration procedures for a specific set of operating parameters. The boundary integration expression to quantify the total flux of fuel crossing the boundary is given by

$$\dot{F} = \iint_{dA_{crossover}} F_{\perp} dA_{crossover} \quad (4.12)$$

where $F_{\perp}$ represents the local normal flux perpendicular to the fuel-to-oxidant interfacial surface ($A_{crossover}$) expressed as

$$-\mathbf{n}.\mathbf{F} = F_{\perp} \quad (4.13)$$

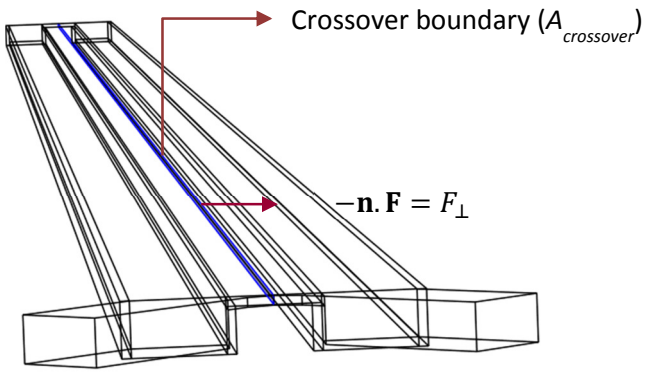

Figure 4.2. Schematic of the surface ($A_{crossover}$) used to compute fuel crossover via boundary integration techniques. The arrow perpendicular to the boundary represents the local flux of fuel that crosses the boundary from the anodic to the cathodic micro flow channel when the cell is in operation.

4.4.5 Velocity Field and Mixing-zone Analysis

Figure 4.3 shows the magnitude of the velocity component in the flow direction (v_y) at a location of 5 mm (y = 5 mm) from the active channel entrance for each structure (AR10, AR5, and AR4). The data represent a cross-sectional line which transverses the center of the bridge from the anodic channel outer side wall (x = -150 µm) to the cathodic channel outer side wall (x = 150 µm). The plots were generated for various flow rates $\dot{V} \in \{10,20,30,40,50,60\}$ µL min^{-1}. For each structure, at a specific input flow rate, a double-parabolic flow developed with a nearly constant low-velocity field in the bridge. Note that the local maxima observed do not represent the absolute maximum velocity of the flow fields, because those occur approximately at the center of the two channels (z = 25 µm) for a given flow rate. The velocity fields for each structure exhibit a mirror effect from anode to cathode due to cell symmetry and the 1:1 flow ratios used in these studies. The low velocity field observed at the bridge is a result of the high proximity between the upper and lower walls at which the no-slip boundary condition applies. The magnitude of the downstream velocity in the bridge region increased from 4 to 20 mm s^{-1} for

AR 10, 15 to 70 mm s^{-1} for AR 5, and 20 to 90 mm s^{-1} for AR 4; upon increasing the flow rates of the individual channels from 10 to 60 μL min^{-1}.

Figure 4.4 captures the concentration profile when the cell (AR 10 structure) is operated with 1 M HCOOH at a flow rate of 60 μL min^{-1}. This concentration field reveals the confinement of the mixing zone along the bridge for the entire flow domain. As listed in the assumptions (Section 4.4.1), due to the appreciable distance between the electrode walls and the point of liquid-liquid mergence (at the middle of the bridge for a 1:1 flowrate ratio), the depletion layers resulting from electrochemical reactions had a minimal impact on the concentration gradient in the mixing zone. Moreover, the Y-shape entry to the cell allows for a volume of unreacted liquids to merge initially at the bridge location and coflow along this catalyst-free zone towards the exit. This set of assumptions enabled us to exclude the reaction kinetics resulting in a simplified version of the model which allows the behavior of the diffusion zone to be studied independently. Figure 4.4(b) illustrates x-z plane concentration snapshots at three locations downstream from the active cell entrance (1, 5 and 9 mm) when the inlet fuel concentration and flow rate were 1 M HCOOH and 60 μL min^{-1}, respectively. Note that the diffusion zone gradually increases in width as flow advances to the exit, but remains confined within the bridge. A similar trend was also noted for AR 5 and AR 4 structures. However, the characteristic mixing zone for each cell operated at the same upstream flow conditions changes in width as elaborated in succeeding sections.

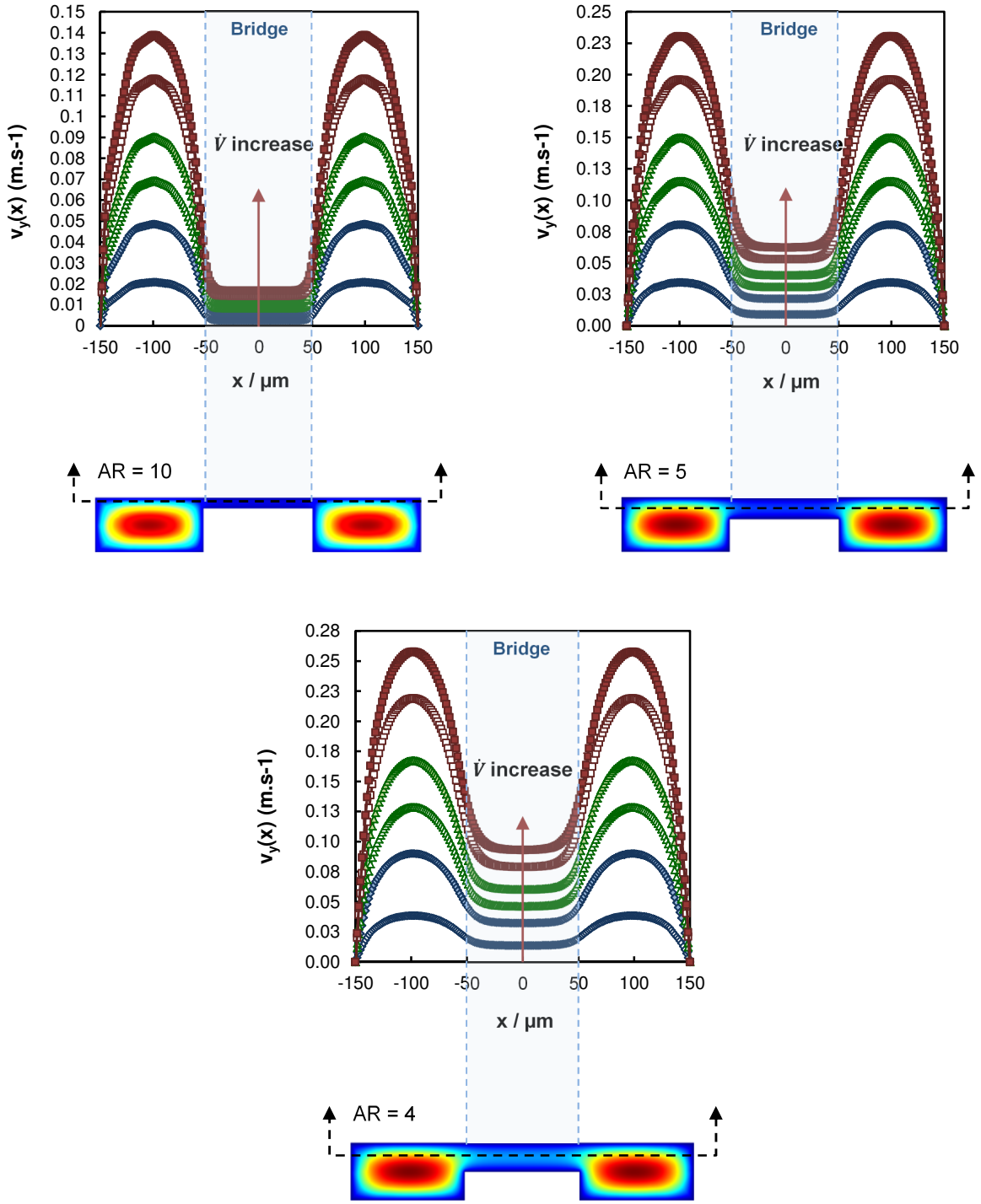

Figure 4.3. Velocity component in the flow direction (v_y) at a location of 5 mm (y = 5 mm) from the cell active-channel entrance for each structure (AR10, AR 5, and AR 4). The data represent a cross-sectional line which transverses the center of the bridge from the anodic channel outer side wall (x = -150 µm) to the cathodic channel outer side wall (x = 150 µm). The plots were generated for various flow rates $\dot{V} \in \{10,20,30,40,50,60\}$ µL min^{-1}, as indicated by the arrow.

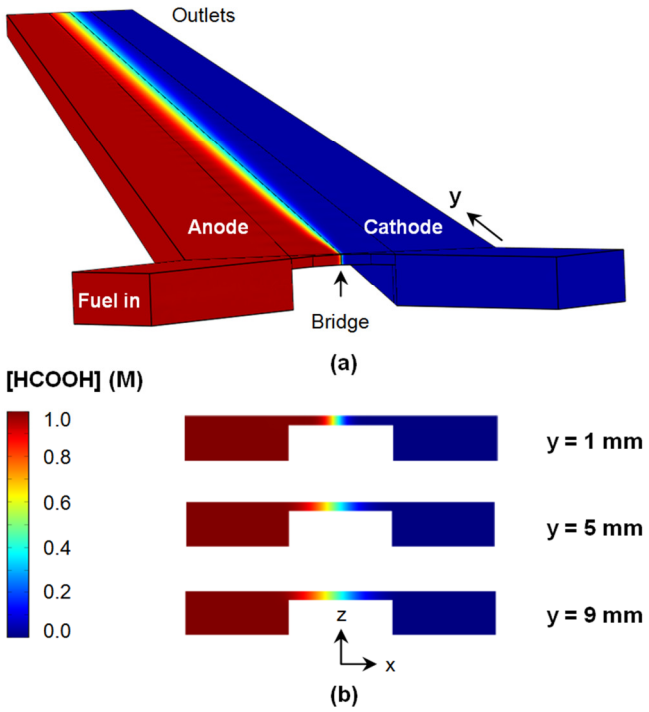

Figure 4.4. Formic acid concentration profiles for a bridge-shaped microchannel geometry (AR 10) when fed with 1 M HCOOH at a flow rate of 60 µL min^{-1}: (a) 3D flow domain; (b) 2D captures with X-Z planes located at three different locations from the cell active-channel entrance (1, 5, and 9 mm in the downstream direction).

The mixing zone width can be controlled by adjusting flow rates [1-2]. Figure 4.5 depicts fuel-concentration profiles at a location of 5 mm (y = 5 mm) from the active cell entrance for each structure (AR 10, AR 5, and AR 4). Similar to Figure 4.3, the data correspond to a cross-sectional line which transverses the center of the bridge from the anodic channel outer side wall (x = -150 µm) to the cathodic channel outer side wall (x = 150 µm). The concentration gradients are evaluated for different flow rates $\dot{V} \in \{10,20,30,40,50,60\}$ µL min^{-1}. In general, the immediate concentration gradient, which characterizes the diffusion zone, became steeper as the flow rate was increased. A similar trend is noted when the bridge aspect ratio is decreased (*i.e,*

when the bridge aperture is increased) but to a higher extent. For instance, at a flow rate of 60 μL min^{-1} this concentration gradient was well confined within the bridge for each structure. In contrast, at lower flow rates (*i.e.,* 10 μL min^{-1}) the concentration gradient broadened and partially interfered with the inner anodic and cathodic channel side walls for AR 10 structure. To utilize the inner channel side walls for electrode (catalyst) integration, interaction with the mixing zone must be avoided. The model suggests the use of higher flow rates and / or lower bridge aspect ratios to reduce the width of the diffusion zone, thereby, improving electrode performance, which may increase fuel utilization. These results are in agreement with the scaling analysis given in Equation (4.2), which indicates that increasing the average velocity results in a thinner diffusion zone. Returning to Figure 4.3, the average velocity at the bridge location moderately increased proportionally to flow rate. Similarly, fuel crossover can be reduced by increasing the Péclet number [2]. According to our data (Figure 4.3), *Pe* (along the bridge location) can be increased from ~ 8×10^1 to ~ 4×10^2 for AR 10, ~ 6×10^2 to ~ 2.8×10^3 for AR 5, and ~ 1×10^3 to ~ 4.5×10^3 for AR 4 using the aforementioned flow rate range. However, increasing *Pe* by increasing the mean velocity may cause the streams to deviate from steady state. Such an onset of hydrodynamic instability has been reported in laboratory experiments and hampers the performance of LFFCs significantly [13]. However, in this work the small dimensions of the bridge enable a more gradual development of the local velocity upon an increase in flow rate, which keeps *Pe* in a safe regime.

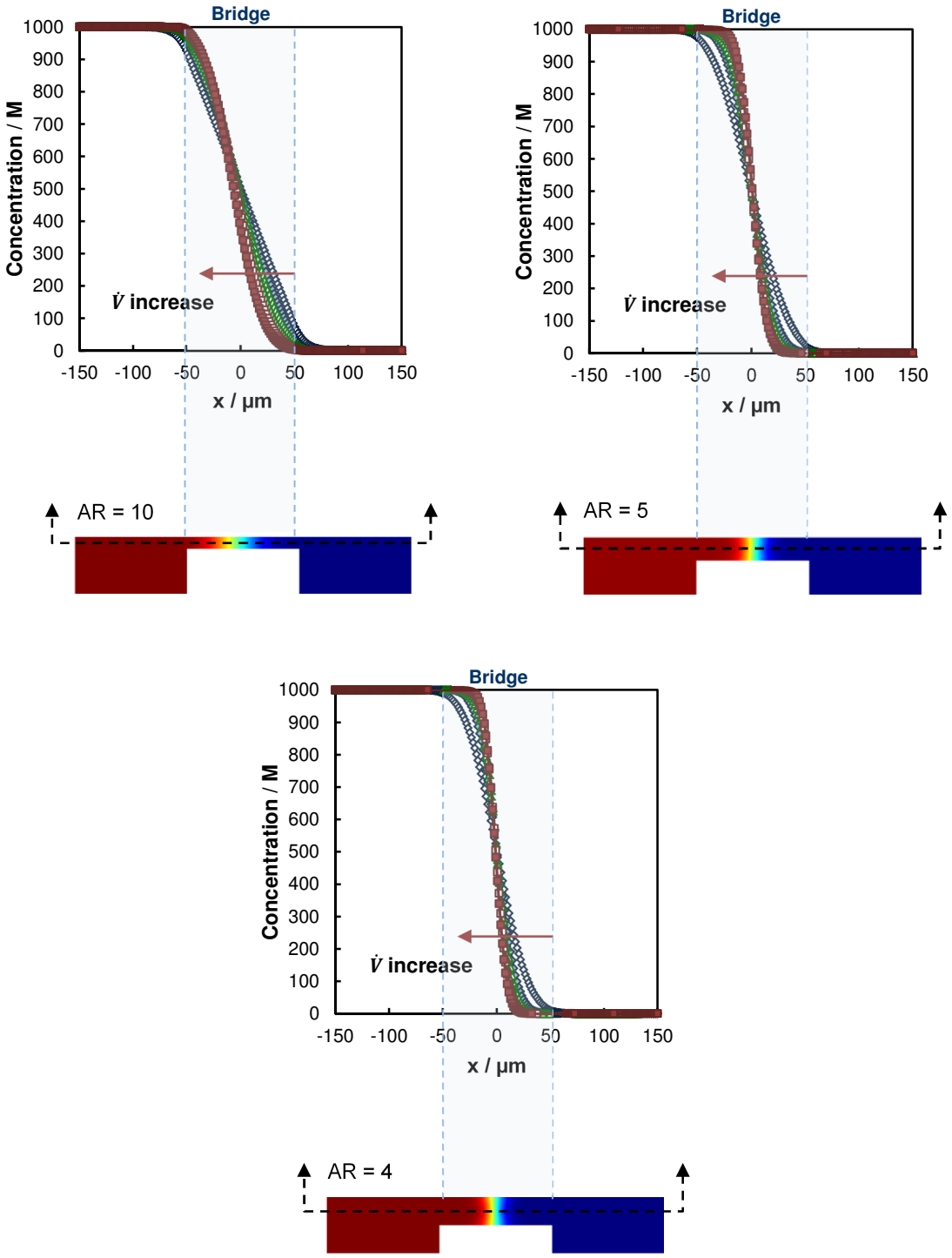

Figure 4.5. Formic acid concentration gradients at a location of 5 mm (y = 5 mm) from the active cell entrance for AR 10, AR5, and AR4. The data correspond to a cross-sectional line which transverses the center of the bridge from the anodic channel outer side wall (x = -150 µm) to the cathodic channel outer side wall (x = 150 µm). The concentration gradients were evaluated for different flow rates $\dot{V} \in \{10,20,30,40,50,60\}$ µL min^{-1}, as indicated by the arrow.

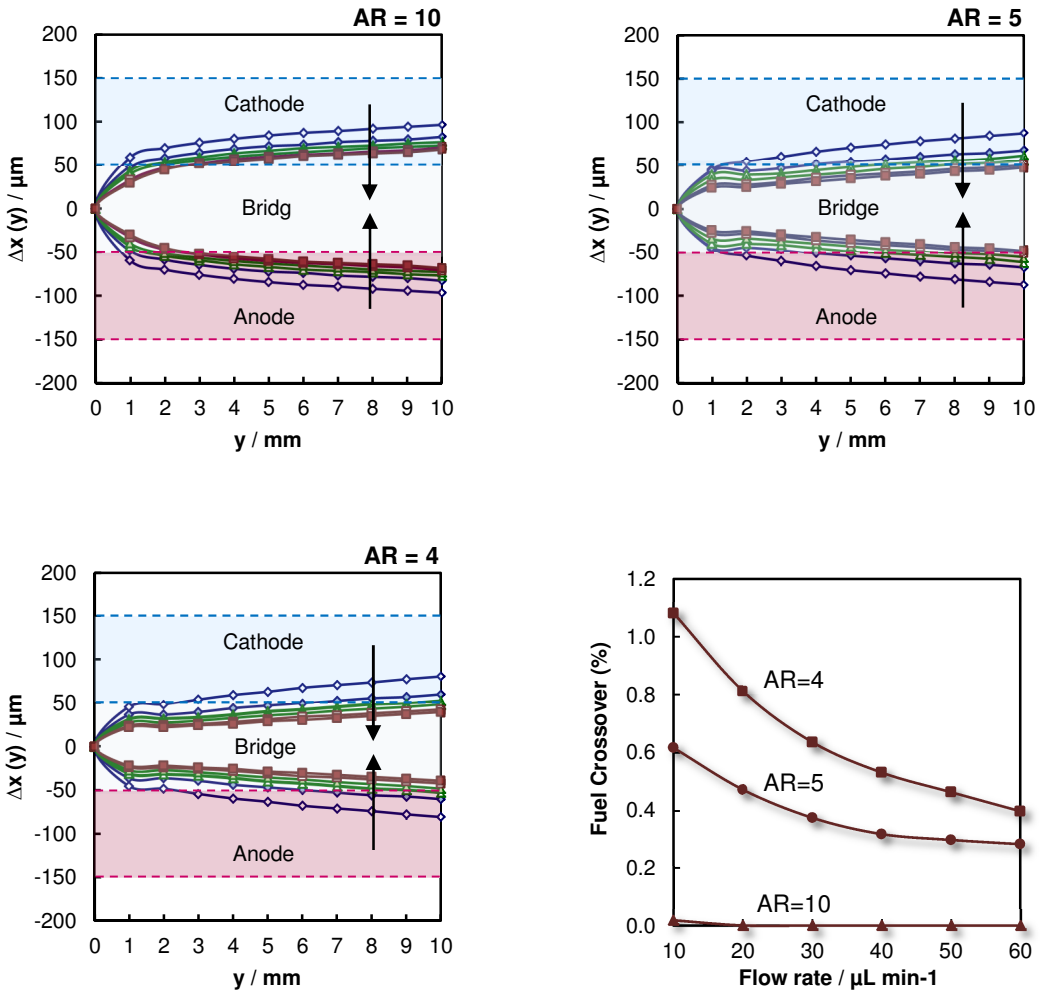

Figure 4.6. Mixing zone width (Δx) for AR 10, AR 5, and AR 4 structures and fuel crossover (in %). The mixing zone width is evaluated for different flow rates $\dot{V} \in \{10,20,30,40,50,60\}$ µL min^{-1}, which increases as pointed by the arrows.

Figure 4.6 indicates the mixing width (Δx) for each structure (AR 10, AR 5, and AR 4) as the reactants advance from the active cell entrance (y = 0 mm) to the active cell exit (y = 10 mm). In general, as flow rate increases the mixing zone width decreases for a given structure. Also, as the bridge aspect ratio decreases (*i.e.,* from AR 10 to AR 4) the mixing zone width decreases the specified flow rate range. For all cases the mixing zone broadens as flow advances to the exit. The thinner mixing zone, for the specified flow rate range, is obtained for AR 4 structure. As

discussed previously, confining the mixing zone within the bridge for the entire flow domain may liberate the active walls to enhance the course of electrochemical reactions, thereby, improving fuel utilization and cell performance. However, by inspecting the fuel crossover vs. flow rate plot in Figure 4.6, the AR 4 structure exhibits the higher percentages in fuel crossover, up to ~1.2 % at the lowest flow rate. These results indicate that opening the structure (*i.e.*, increasing the bridge height) may help in attenuating the mixing zone at the expense of fuel crossover. This conflicting issue will be clarified in the next section (the complete fuel cell model) by computing new values for reactant crossover and study their effect on overall cell performance.

4.5 Fuel Cell Model

To assess the I-V characteristics (*i.e.,* performance) of the μLLFCs via numerical simulations, the mixing zone model was extended to reveal the voltage profile due to the current generated at the electrodes when the cell is in operation. Therefore, Charge Balance and Votler-Bulmer equations are coupled in this section to complete the model. These equations will be discussed in details in the succeeding sections.

To complete the fuel cell model new subdomains are added to account for additional physics. The overall computational domain now consists of four sub-domains: the anodic and cathodic micro flow channels and the anodic and cathodic porous electrodes (Figure 4.7). The reactants (*i.e.,* formic acid and potassium permanganate solutions) flow through the anodic and cathodic micro flow channels, respectively, get into superficial contact with the porous electrodes, where electrochemical reactions occur, but do not flow through these subdomains. The electrodes are modeled as porous sub-domains that include the catalyst layer (*i.e.,* Palladium) and current

collector (*i.e.,* Gold), lumped together. The governing equations and boundary conditions that apply to all sub-domains are discussed in the next sections. Physical properties and input parameters used in the simulations are included in Appendix A.

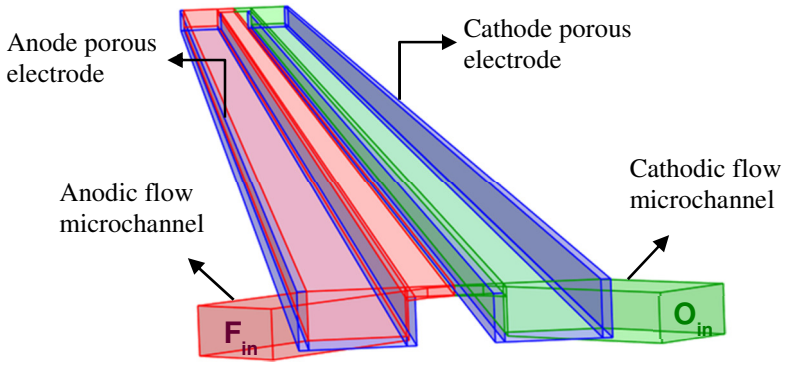

Figure 4.7. Schematic of the overall 3-D computational domain which consists of four subdomains, namely, anodic and cathodic micro flow channels and anodic and cathodic porous electrodes.

4.5.1 Assumptions

The set of assumptions formulated for the mixing zone model (Section 4.4, i-vi) still apply for the complete fuel cell model. Therefore, we only state here additional assumptions to obtain simplified versions of the remaining governing equations (Section 4.5.2.).

(vii) Fuel and oxidant solutions get into superficial contact with the porous (reactive) electrode walls but do not enter or flow through these sub-domains. Therefore, electrochemical reactions can be conveniently modeled by imposing fluxes (as boundary conditions) using Faradays law and Butler-Volmer equations.

(viii) Fuel and oxidant (*i.e.,* formic acid and potassium permanganate) are supported in acidic electrolyte and the concentration of hydrogen ions was assumed to be uniform through the micro flow channels.

(ix) The transport of protons from the anodic to the cathodic micro flow channel is by migration only.

(x) The current collectors and catalyst layers are lumped into single solid-phase porous sub-domains, namely, the anode electrode and the cathode electrode.

(xi) Archie's Law applies in the porous electrodes to obtain an effective conductivity value.

4.5.2 Governing Equations and Boundary Conditions

The governing equations established for the mixing zone model (Section 4.4) still apply for the present case. For instance, the flow characteristics (*i.e.,* velocity profiles) are still unchanged because the solutions are independent of mass and/or charge transport. Therefore, the Continuity and Navier-Stokes equations and corresponding boundary conditions are not reviewed in this section. Indeed, the velocity solutions discussed in Section 4.4 are used to complete the fuel cell model. In contrast, the concentration fields were resolved using the diffusion-convection equation only since oxidation and reduction electrochemical reactions were neglected. Now for the complete fuel cell model we account for electrode reactions and the mass transport modes that account for these new physics are reviewed and modified accordingly. In the anodic and cathodic micro flow channels the transport of species can be described by

$$\nabla.(-\mathrm{D}\nabla\mathrm{c} + \mathrm{c}\mathbf{u}) = R_{rxn} \tag{4.14}$$

where c is the concentration of a species, D indicates the corresponding diffusivity, and R_{rxn} is the reaction rate. Using assumption (vii), the reaction term (R_{rxn}) can be set to zero and the electrochemical reactions can be modeled by imposing fluxes at the reactive walls. The fluxes at these reactive walls can be used as boundary conditions

$$-\mathbf{n}.\mathbf{N} = N_0 \tag{4.15}$$

where **N** is given by

$$\mathbf{N} = -D\nabla c + c\mathbf{u} \tag{4.16}$$

and N_0 is the flux of fuel or oxidant coming out of the wall (*i.e.,* consumed at the reactive wall) in the perpendicular direction. **N** and **n** are flux and normal vectors, respectively. The amount of fuel and oxidant that is consumed at the anode and cathode electrode walls (represented in this model by fluxes) must be appropriately quantify using Faraday's Law

$$N_0 = \frac{J_n}{nF} \tag{4.17}$$

where J_n is the current generated at the electrode surface due to oxidation or reduction electrochemical reactions, n the number of moles involved the reactions and F is the Faraday constant. Note that the imposed fluxes that represent electrochemical reactions at the electrode surfaces are function of the concentration of the reactant of interest and the current generated

$$N_0 = f(J_n, c) \tag{4.18}$$

Quantifying the current generated at each electrode surface is possible by applying Butler-Volmer equation for electrode kinetics as elaborated below. The remaining boundary conditions that apply to the anodic and cathodic micro flow channels in terms of mass transport are consistent with those already established in Section 4.4 and hence are not reviewed in this section.

Charge conservation

Using assumptions (viii) and (xi) (Section 4.5.1.) the transport of charge species across the different sub-domains can be modeled using the potential equation found in the conductive media dc application mode of COMSOL Multiphysics. The current generated at the electrodes due to electrochemical reactions can be treated as electronic and ionic currents which are equivalent but opposite in sign. The ionic current evolving from the migration of protons is transported through the electrolyte from the anodic micro flow channel to the cathodic micro flow channel. In our model, the electronic current evolving from the electrons flow enters the cathode porous electrode sub-domain to escape the cell and is input into the anode electrode subdomain where it transforms into ionic current to complete the circuit.

The general current transport (electronic and ionic) is governed by the equation for conservation of charge

$$\nabla.(-\sigma\nabla\varphi) = A_s S_\varphi \tag{4.19}$$

where σ is the conductivity of the layer or sub-domain of interest, φ is the local potential, A_s is the electrochemical surface area, and S_φ is the electrical current source term. In our model we set the volumetric terms (sources) to zero to work on a surface basis. Working on as surface basis is possible as we are setting the current generated at the electrodes as boundary conditions. Therefore, the right side term of equation (4.19) vanishes

$$\nabla.(-\sigma\nabla\varphi) = 0\,. \tag{4.20}$$

Equation (4.20) applies for all four sub-domains as elaborated below. The electronic current at the solid porous electrodes, can be modeled by modifying the charge conservation equation

$$\nabla.(-\sigma_{eff}\nabla\varphi_s) = 0 \tag{4.21}$$

where σ_{eff} is the effective conductivity of the porous medium (*i.e.,* catalyst layer) and φ_s the

solid-phase local potential. To recreate the physical state of the porous electrodes we assume that these sub-domains are saturated with liquid electrolyte and the conductivity must be an effective value. In this model, we made use of a power law formula known as Archie's Law to assess the effective conductivity of the porous electrodes. In geophysics, this relationship is used to approximate the electrical conductivity of isotropic, liquid-saturated rocks of complicated microporous structure. Adapting Archie's Law to our case, the effective conductivity of the porous electrodes is approximated as follow

$$\sigma_{eff} = \sigma_0(1-\varepsilon)^m \tag{4.22}$$

where σ_0 is the electrical conductivity of the non-porous material (*i.e.,* pure Palladium), ε is the porosity (~ 0.5 for high surface area catalyst), and m, which is determined empirically, is related to the tortuosity of the porous material. Common values for m range from 1.8 -2.5.

The following boundary conditions apply to the porous electrodes at the outer walls

$$\varphi_s = 0\,, \qquad \text{anode electrode} \tag{4.23}$$

$$\varphi_s = V_{cell}\,, \qquad \text{cathode electrode.} \tag{4.24}$$

If we arbitrarily set the solid-phase potential at the anode electrode to zero, the cathode electrode solid-phase potential represents the operating cell voltage (V_{cell}). At the active walls of the porous electrode, where electrochemical reactions occur, the following boundary conditions apply to account for the current generated

$$-\mathbf{n}.\mathbf{J} = J_n \tag{4.25}$$

where $\mathbf{J}$ is the current vector and J_n is the normal local current produced at the electrodes (J_{n_a} for the anode and J_{n_c} for the cathode), which are determined using the Butler-Volmer equations as defined later in this section. For all the remaining electrode walls current insulation applies

$$\mathbf{n}.\mathbf{J} = 0 \tag{4.26}$$

Similarly, the ionic current in the anodic and cathodic micro flow channels can be modeled using the following charge conservation equations

$$\nabla.\left(-\sigma_{e_a}\nabla\varphi_e\right)=0, \quad \text{anodic micro flow channel} \tag{4.27}$$

where σ_{e_a} is the electrical conductivity of the liquid electrolyte in the anodic micro flow channel and φ_e is the local liquid-phase potential. Similarity, at the cathodic micro flow channel the charge conservation is given by

$$\nabla.\left(-\sigma_{e_c}\nabla\varphi_e\right)=0, \quad \text{cathodic micro flow channel} \tag{4.28}$$

where σ_{e_c} is the electrical conductivity of the liquid electrolyte in the cathodic micro flow channel. The boundary conditions in the anodic and cathodic micro flow channels are stated for active (*i.e.,* reactive) and inactive walls

$$-\mathbf{n}.\mathbf{J}= J_n \qquad J_{n_a}\text{, anode active wall} \qquad -J_{n_c}\text{, cathode active wall} \tag{4.29}$$

$$\mathbf{n}.\mathbf{J}=0\text{,} \qquad \text{all inactive (non-reactive) walls.} \tag{4.30}$$

Butler-Volmer equations

In previous discussions we have stated that the current generated at the electrodes can be used as boundary conditions to resolve the current and voltage profiles in each sub-domain (*i.e.* porous anode and cathode electrodes and anodic and cathodic micro flow channels). The Butler-Volmer equations describe how the electrical current on an electrode depends on the electrode potential, considering that both a cathodic and an anodic reaction occur on the same electrode**.** For the anodic electrochemical reaction

$$J_{n_a}=i_{0_a}\frac{C}{c_{ref}}\left(\exp\left(\frac{-\propto_{a_a}F\eta_a}{RT}\right)-\exp\left(\frac{-\propto_{c_a}F\eta_a}{RT}\right)\right); \qquad c=c_{HCOOH} \tag{4.31}$$

while for the cathodic electrochemical reaction

$$J_{n_c} = i_{0_c} \frac{C}{c_{ref}} \left(\exp\left(\frac{-\alpha_{a_c} F \eta_c}{RT}\right) - \exp\left(\frac{-\alpha_{c_c} F \eta_c}{RT}\right) \right); \qquad c = c_{MnO_4^-} \tag{4.32}$$

where i_{0_a} and i_{0_c} are the anode and cathode exchange current densities, c is the local reactant concentration, c_{ref} is the reference concentration, α_{a_a} and α_{c_a} are the anodic and cathodic charge transfer coefficients of the reaction at the anode electrode, α_{a_c} and α_{c_c} are the anodic and cathodic charge transfer coefficients of the reaction at the cathode electrode, η_a and η_c are the anode and cathode overpotentials, R is the ideal gas constant, and T is the temperature which is room temperature for the present case. The local concentration (c) which is factored in the equations enables us to determine the depletion regions as the reactants of interest are consumed.

The anode overpotential is defined

$$\eta_a = \varphi_s - \varphi_e - \varphi_{rev_a} \tag{4.33}$$

and the cathode overpotetial

$$\eta_c = \varphi_s - \varphi_e - \varphi_{rev_c} \tag{4.34}$$

where φ_s is the solid phase-potential from the solid porous electrodes, φ_e is the electrolyte or liquid-phase potential from the micro flow channels, φ_{rev_a} is the anode reversible potential (*i.e.,* the anode potential when formic acid is flowing over Pd-catalyst at open circuit conditions) and the oxidation reaction is at equilibrium, and similarly, φ_{rev_c} is the cathode reversible potential when the reduction reaction is also in equilibrium at open circuit conditions.

An initial "guess" condition was applied to assist convergence

$$\varphi_s \rightarrow V_{cell} \tag{4.35}$$

the solid-phase potential at the cathode electrode can be approximated to the operating cell potential (V_{cell}) due to the high electrical conductivity of the porous electrode sub-domains (porous Pd catalyst on gold).

4.6 Meshing Technique

Figure 4.8 shows the mesh selected for all structures (*i.e.,* AR 10, AR 5, and AR 4). The mesh is extremely fine in x-z plane to capture large gradients while swept in the y direction to minimize the total amount of elements (e.g., AR 4 = 39,703 elements).

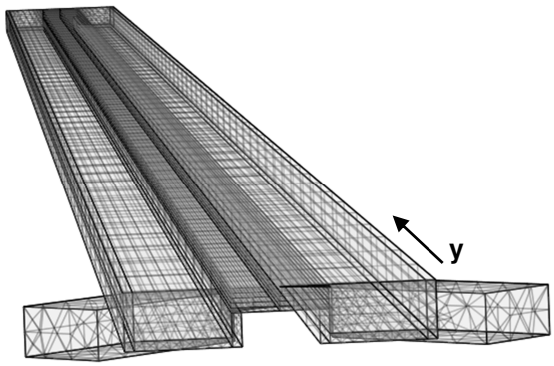

Figure 4.8. Swept mesh for AR 4 structure. The mesh is extremely fine in x-z plane to capture large gradients while swept in y direction to minimize the total amount of elements.

4.7 Solution Procedures

The computations were performed using a Windows computer (64-bit operating system) with Intel (R) Xeon CPU, X5450 3.0 GHz (2 processors), and 32.0 GB of RAM. First, the Navier-Stokes equation and charge balance for the porous electrodes were solved followed by the species balance for anodic and cathodic micro flow channels and charge balance for the electrolyte. At an intermediate step the solution was stored and used to solve the entire set of equations with the already established boundary conditions. The total computing time for all stages was approximately ~16 minutes for one value of voltage scan.

4.8 Determination of Cell Performance

Once the model is solved we proceed to determine the I-V characteristic of the μLFFCs with bridged-shaped microchannel cross-section of different aspect ratios (*i.e.,* AR 10, AR 5, and AR 4). The overall performance of the cells is presented via polarization curves for different operating conditions. For each point on the polarization curve, the cell operating voltage (V_{cell}) is taken as the solid-phase potential assigned to the cathode when the boundary conditions are established to solve the potential equations at the electrode sub-domains since the anode is arbitrarily set to zero. The current produced by the cell is determined during the post-processing tasks by integrating the normal local current over the active (reactive) cathodic microchannel walls. This evaluation is performed at the cathode side given that the cell is cathode limited. Therefore, when the cell is in operation the circuit balances and the anode and cathode operate at the same current value, *i.e.,*

$I_a = I_c$ at nominal operating cell voltage (V_{cell}) (4.36)

where I_a and I_c are the total anode and cathode current, respectively. The boundary integration expression at the cathode is given as

$$I_c = \iint_{A_1} J_{n_c} dA_1 + \iint_{A_2} J_{n_c} dA_2 + \iint_{A_3} J_{n_c} dA_3 \quad (4.37)$$

where J_{n_c} is the normal local current and A_1, A_2, and A_3 are the cathodic micro flow channel active (catalytic) areas. Once the total current value is obtained, we normalized it by the corresponding cathode geometrical area to obtain current density. Figure 4.9 shows how the boundary integration is performed in COMSOL Multiphysics.

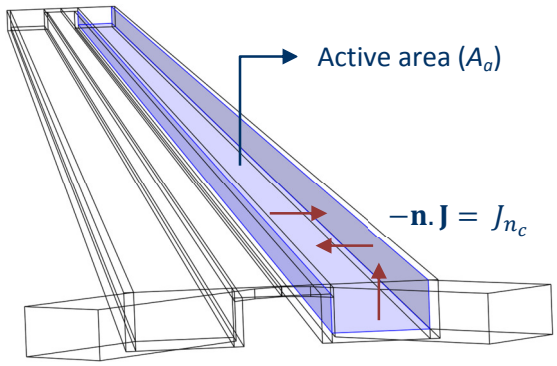

Figure 4.9. Schematic of cathode active (reactive) surface area (A_a) used to compute the current generated via boundary integration techniques. Once the total current generated (I_c in equation (4.37) is determined, the value is normalized over the total geometrical area to obtain current density.

4.9 Determination of Fuel utilization

In the experiments, the μLFFCs were operated with 1.0 M HCOOH. Due to the low range of current densities observed in these single micro-fuel cells, fuel utilization is modest at this concentration. Therefore, for the evaluation of fuel utilization we have selected the highest power producing micro-fuel cell (*i.e.,* AR 4). Fuel utilization is evaluated at the anodic micro flow channel when running the model at a nominal cell voltage (V_{cell}) of 0.7. Low and high fuel flow rates (10 and 60 μL min^{-1}, respectively) are evaluated representing the cases of high and low fuel residence times within the anodic micro flow channel. The inlet fuel concentration is always fixed to 1M.

Fuel utilization (%) is given by

$$\Omega = \frac{\dot{n}_{f_{in}} - \dot{n}_{f_{out}}}{\dot{n}_{f_{in}}} * 100 \qquad (4.38)$$

where $\dot{n}_{f\,in}$ and $\dot{n}_{f\,out}$ are the fuel inlet and outlet molar flow rates, respectively. These values are extracted in COMSOL via integration techniques performed at the inlet and outlet boundaries of the anodic micro flow channel.

4.10 Oxidant Consumption Rate Determination

The oxidant consumption rate is also an important parameter to evaluate given the great incidence of cathode limited cells including the present case. To determine the oxidant consumption rate we have also selected the highest power producing micro-fuel cell (*i.e.,* AR 4). The oxidant consumption rate is evaluated at the cathodic micro flow channel when running the model at a nominal cell voltage (V_{cell}) of 0.7. Low and high oxidant flow rates (10 and 60 μL min^{-1}, respectively) are evaluated which represent the cases of high and low oxidant residence times within the cathodic micro flow channel. Also, low and high values of oxidant inlet concentration (20 mM and 144 mM, respectively) were considered for the calculations.

The oxidant consumption rate can be expressed as

$$\lambda = \frac{\dot{n}_{o\,in} - \dot{n}_{o\,out}}{\dot{n}_{o\,in}} \tag{4.39}$$

where $\dot{n}_{o\,in}$ and $\dot{n}_{o\,out}$ are the oxidant inlet and outlet molar flow rates, respectively. These values are extracted in COMSOL via integration techniques performed at the inlet and outlet boundaries of the cathodic micro flow channel.

4.11 Determination of Power Losses

Ancillary (pump)

To obtain high net cell performance the power losses associated with the mode of reactant delivery must be as low as possible. Power losses associated with active reactant delivery (*i.e*., pumps) can be approximated by using the pressure drop solutions. The cell pressure drop was determined for the three cells (*i.e.,* AR10, AR5, and AR4) operating at different reactant flow rates ($\dot{V} \in \{10,20,30,40,50,60\}$ μL min^{-1}). The corresponding cell pressure drop values are included in Appendix A.

Crossover current

Fuel crossover is the phenomenon where the fuel bleeds from the anodic micro flow channel to reach the catalytic walls of the cathodic micro flow channel. This phenomenon reduces fuel utilization, results in a detrimental mixed current, and poisons the cathode catalyst which decreases the efficiency of the oxidant reduction reaction. Oxidant crossover is also possible especially for cells that utilize liquid oxidant to carry out the reduction reaction in the cathode. Here we quantify fuel and oxidant crossover as explained in Section 4.4.4. and convert this data into crossover current density. We have selected the micro-fuel cell that exhibits the highest fuel crossover (*i.e.,* AR 4) to determine the crossover current. The data was analyzed for various cell operating parameters. Low and high reactant flow rates of 10 and 60 μL min^{-1}, low and high oxidant concentration of 20 and 144 mM, and fixed fuel concentration of 1M. The operating cell voltage is V_{cell} = 0.7 V. To compute crossover current density, we assume that the amount of fuel that crosses to the cathodic micro flow channel is completely oxidized at the catalyst layer. Similary, we assume that the amount of oxidant that crosses to the anodic micro flow

channel is completely reduced at the catalyst layer. Therefore, crossover current due to fuel and oxidant crossover can be computed using the following formulas

$$I_{co_f} = M_f N_{e_o} F \tag{4.40}$$

$$I_{co_o} = M_o N_{e_r} F \tag{4.41}$$

where M_f is the molar flux of fuel that crosses to the cathodic micro flow channel, M_o is the molar flux of oxidant that crosses to the anodic micro flow channel, N_{e_o} is the number of electrons involved in the oxidation reaction, N_{e_r} is the number of electrons involved in the reduction reaction, and F is the Faraday constant. Once crossover currents due to fuel or oxidant crossover are determine, we normalize these values by the geometrical active surface area of the cell to obtain crossover current density.

4.12 Results

4.12.1 Model Validation

Figure 4.10 (upper plot) shows polarization (open squares and circles) and power-density (filled squares and circles) curves for a μLFFC (AR 10) already reported in literature [3]. The plot shows the performance of the cell when operated with 1 M HCOOH and 144 mM $KMnO_4$ at a flow rate of 60 μL min^{-1}. According to this plot the model fairly agrees with the experimental data. At low potentials the model performance prediction departs somewhat from the experimental data due to secondary reduction reactions that may occur. In acidic solutions, the permanganate reduction reaction is prone to yield insoluble MnO_2 at low potentials (< 0.5 V). Therefore, mass transport issues at the cathode will limit the overall performance at low potentials as noted from the experimental polarization curve. Since the fuel cell model does not account for alternative electrochemical reduction pathways the model-to-experimental fit is

somewhat loose at low potentials. However, in practical applications, fuel cells are operated at a nominal voltage of (~ 0.6 to 0.8 V) where the model predictions are still in agreement with experimental data. Therefore, we have characterized all our cell structures (AR 10, AR 5, and AR 4) at operating voltages above 0.5 V. Figure 4.10 (lower insert) illustrates a 2-D (x-z) plane snapshot of the oxidant (*i.e.,* permanganate) concentration field at a location of y = 9 mm from the active cell entrance. At this location, the depletion region resulting from oxidant consumption at the electrode walls is more apparent for the specified set of operating conditions. The mixing zone (at the bridge location) behaves as previously discussed in Section 4.4.4. In the next section we analyze the performance of all cells structures at various operating parameters. Since the μLFFCs were proved to be cathode limited we always link performance to the concentration field of the oxidant. Fuel concentrations profiles are provided in Section 4.12.4 to address the topic of fuel utilization.

4.12.2 Cell Performance

In this section the performance of the μLFFCs (*i.e.,* AR 10, AR 5, and AR 4) is presented using polarization (I-V curves). Mass transport limitations are presented via oxidant concentration fields since the cell performance is consistently limited by the cathode reaction.

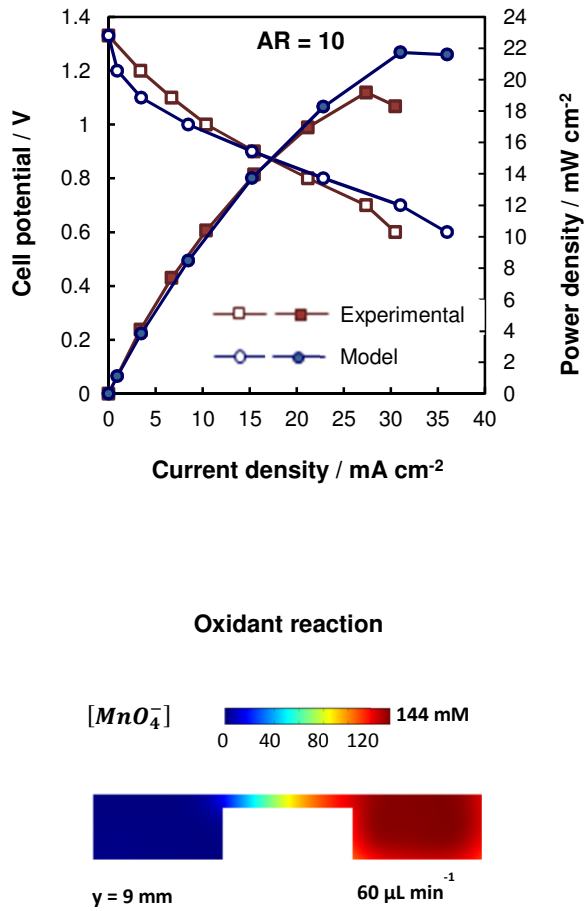

Figure 4.10. The upper plot illustrates polarization (open squares and circles) and power-density (filled squares and circles) curves for the AR 10 cell structure when operating with 1 M HCOOH and 144 mM $KMnO_4$ at a flow rate of 60 µL min^{-1}. The model (blue curves) is compared with the experimental data [3]. The lower insert illustrates a 2-D (x-z) plane snapshot of the oxidant concentration field at a location of y = 9 mm from the active cell entrance.

Figure 4.11 illustrates oxidant (*i.e.,* permanganate) concentration profiles for AR 10 cell structure when fed with 20 mM $KMnO_4$ at a flow rate of 10 or 60 µL min^{-1}. A 3D flow domain is shown in the left upper insert of the figure along with 2D snapshots (x-z planes) located at three different locations from the cell active-channel entrance (1, 5, and 9 mm in the downstream direction) as shown in the left lower insert. The oxidant concentration fields revealed two important zones, namely mixing and depletion. At this low oxidant concentration (*i.e.,* 20 mM

$KMnO_4$) the depletion regions that result from the electrochemical reduction reactions become more apparent compared to the AR 10 cell structure running at higher oxidant concentration (Section 4.5.1). As noted from the 2-D snapshots, the depletion layers increase in thickness as reactants advance to the exit (from y = 1 to y = 9 mm). By increasing the flow rate from 10 to 60 μL min^{-1} the depletion thickness decreases. For the AR 10 cell structure the model predicted a maximum power density of ~ 13 and ~17 mW cm^{-2} at a flow rate of 10 and 60 μL min^{-1}, respectively. For this specific case, an increase in reactant flow rate positively affects overall cell performance. This increase in power density may be associated with changes in the depletion layer as observed from the 2-D snapshots. At high flow rate we obtain thinner depletion regions which may enhance the reactant transport to the active walls of the cell as the concentration gradient becomes steeper. In contrast, by inspecting the mass transport region of the I-V curves (*i.e.,* high current density case), the performance drops considerably for the low flow rate case which exhibits a thicker depletion layer. When a thicker depletion layer is formed, not only the oxidant available in the cathodic microchannel is minimum but it struggles to reach the active walls of the channel as the concentration gradient has been lessened. Therefore, the overall cell performance was improved by operating the cell at higher flow rate (60 μL min^{-1}).

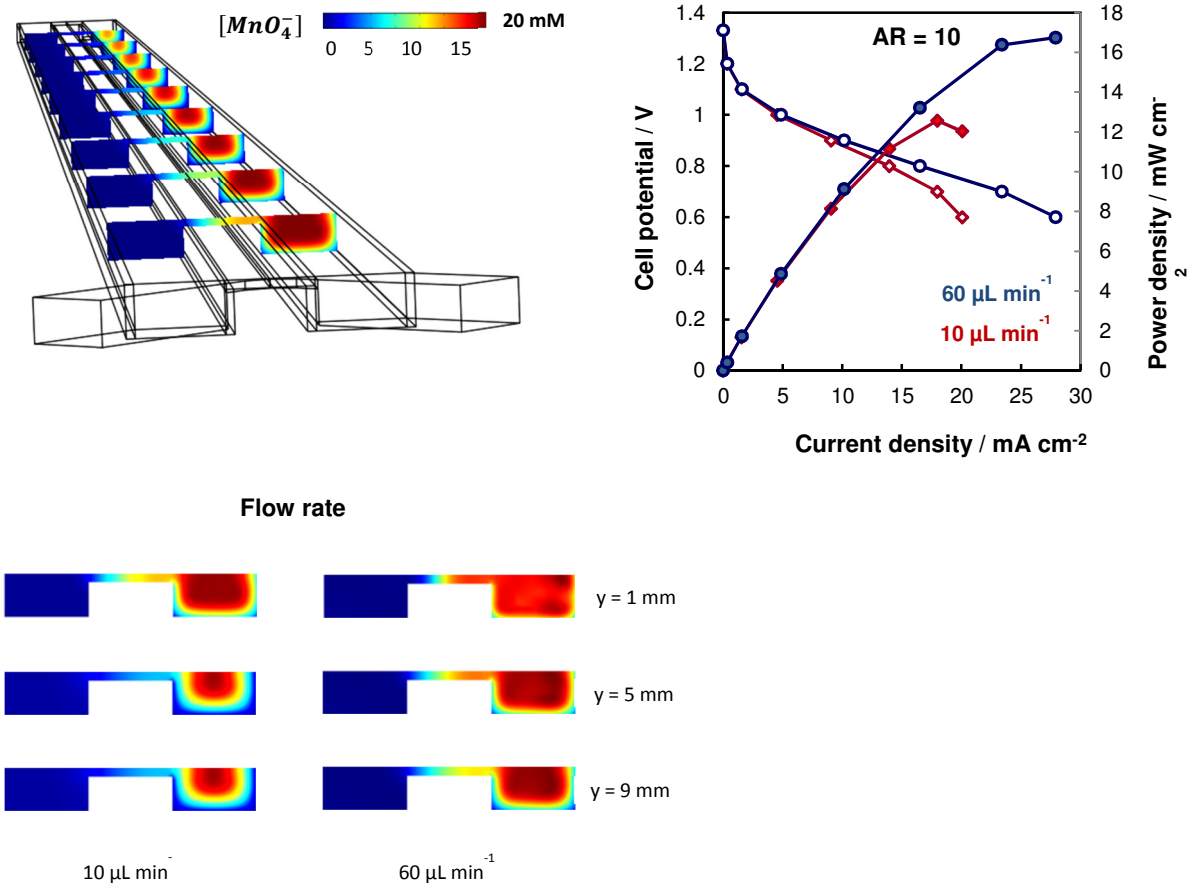

Figure 4.11. COMSOL captures (left inserts): oxidant (*i.e.,* permanganate) concentration profiles for AR 10 cell structure when fed with 20 mM $KMnO_4$ at a flow rate of 10 or 60 µL min^{-1}. The 3D flow domain (left upper insert) and 2D snapshots (left lower insert) with x-z planes located at three different locations from the cell active-channel entrance (1, 5, and 9 mm in the downstream direction). Right upper insert: polarization (open squares and circles) and power-density (filled squares and circles), as predicted by the model.

Figure 4.12 (upper plot) shows polarization (open squares and circles) and power-density (filled squares and circles) curves for AR 10 cell structure. The plot shows the performance of this cell when operated with 1 M HCOOH and high oxidant concentration of 144 mM $KMnO_4$ at a flow rate of 10 or 60 µL min^{-1}. The model predicted peak power densities of ~18 and ~22 mW cm^{-2} when the cell is operated at a flow rate of 10 and 60 µL min^{-1}, respectively. As previously elaborated, this improvement in power density may be attributed to changes in the depletion region as reactant flow rate is increased. At higher flow rates (*e.g.,* 60 µL min^{-1}) the

concentration gradient that characterizes the depletion region becomes steeper (Figure 4.12, lower insert). Steeper concentration gradients enhance the flux of reactant to the electrode walls, thereby, improving the course of the electrochemical reduction reaction for higher performance.

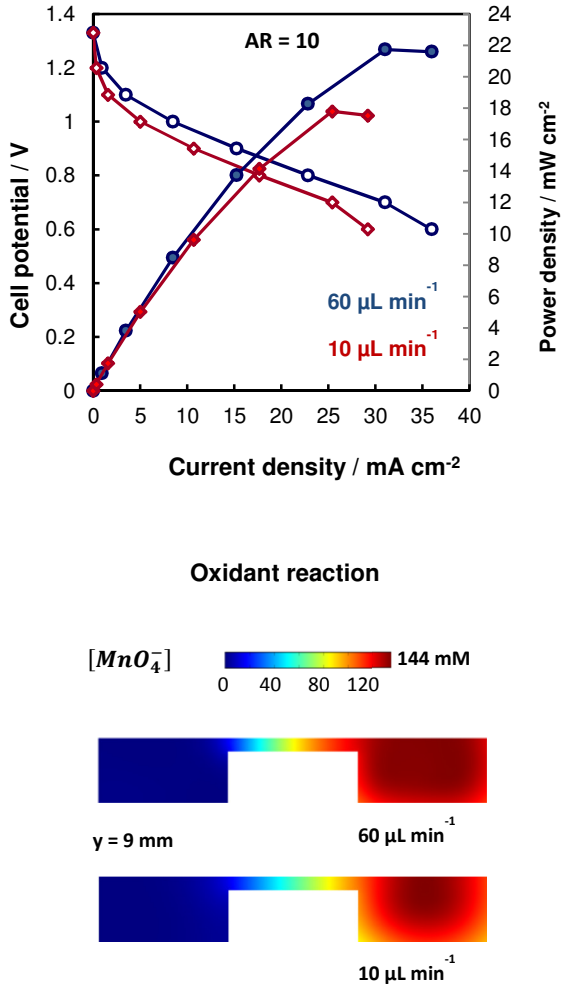

Figure 4.12. Polarization (open squares and circles) and power-density (filled squares and circles) curves for the AR 10 cell structure when operating with 1 M HCOOH and 144 mM $KMnO_4$ at low and high flow rates (10 and 60 µL min^{-1}, respectively) (upper insert). 2-D (x-z) plane snapshot of the oxidant concentration field at a location of y = 9 mm from the active cell entrance (lower insert).

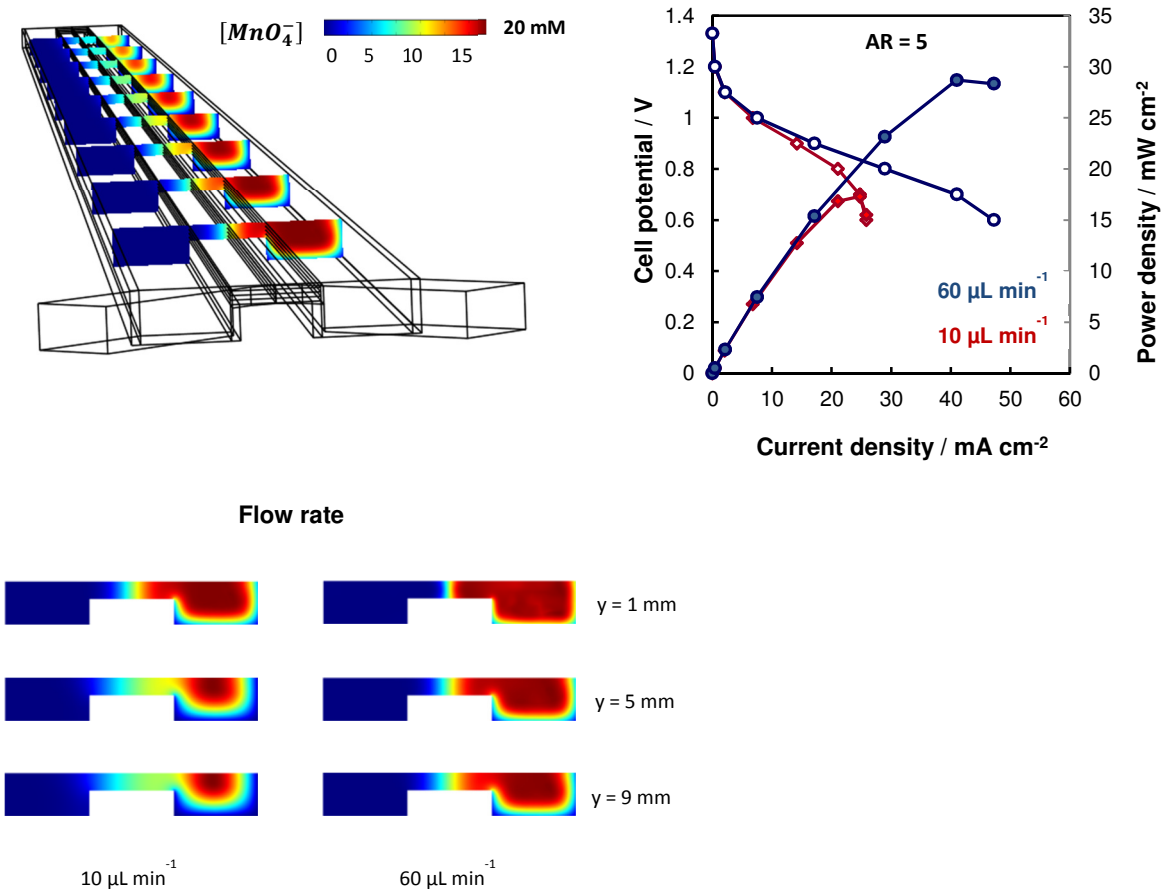

Figure 4.13. COMSOL captures (left inserts): oxidant (*i.e.,* permanganate) concentration profiles for AR 5 cell structure when fed with 20 mM $KMnO_4$ at a flow rate of 10 or 60 µL min^{-1}. The 3D flow domain (left upper insert) and 2D snapshots (left lower insert) with x-z planes located at three different locations from the cell active-channel entrance (1, 5, and 9 mm in the downstream direction). Right upper insert: polarization (open squares and circles) and power-density (filled squares and circles), as predicted by the model.

Figure 4.13 illustrates oxidant (*i.e.,* permanganate) concentration profiles for AR 5 cell structure when fed with 20 mM $KMnO_4$ at a flow rate of 10 or 60 µL min^{-1}. A 3D flow domain is shown in the left upper insert of the figure along with 2D snapshots (x-z planes) located at three different locations from the cell active-channel entrance (1, 5, and 9 mm in the downstream direction) as shown in the left lower insert. For the AR 5 cell structure the model predicted a maximum power density of ~ 17 and ~28 mW cm^{-2} at a flow rate of 10 and 60 µL min^{-1}, respectively. As in previous cases, an increase in reactant flow rate improves cell performance

which is attributed to changes in the depletion regions as elaborated in previous discussions. Also, an improvement in overall cell performance at low oxidant concentration (*i.e.,* 20 mM $KMnO_4$) is noted when the bridge aspect ratio decreases from AR = 10 to AR = 5. Decreasing the bridge aspect ratio implies a bigger aperture for protons transport (*i.e.,* increased bridge height) which reduces the cell resistance, thereby, improving cell performance.

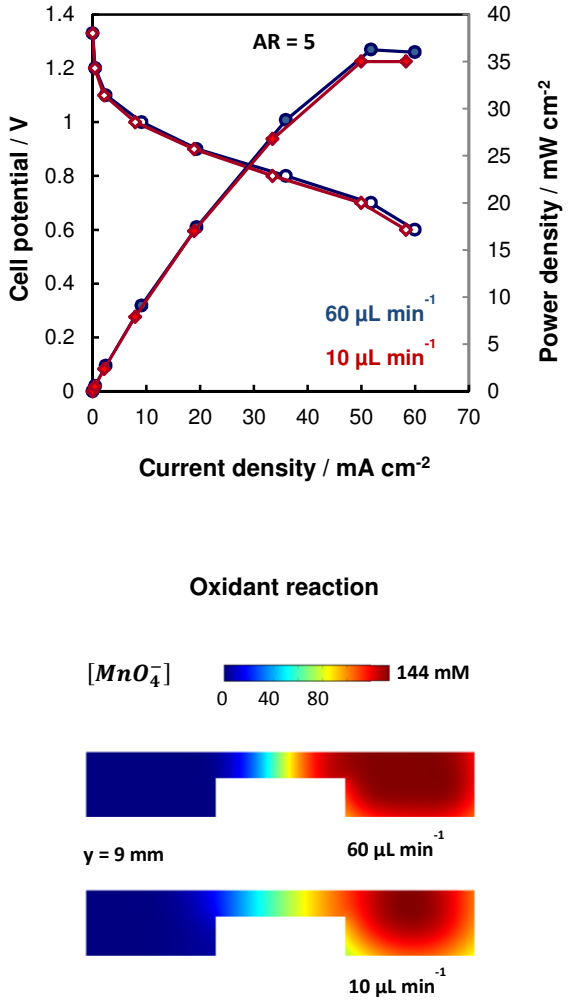

Figure 4.14. Polarization (open squares and circles) and power-density (filled squares and circles) curves for the AR 5 cell structure when operating with 1 M HCOOH and 144 mM $KMnO_4$ at low and high flow rates (10 and 60 µL min^{-1}, respectively) (upper insert). 2-D (x-z) plane snapshot of the oxidant concentration field at a location of y = 9 mm from the active cell entrance (lower insert).

Figure 4.14 (upper plot) shows polarization (open squares and circles) and power-density (filled squares and circles) curves for AR 5 cell structure. The plot shows the performance of this cell when operated with 1 M HCOOH and high oxidant concentration of 144 mM $KMnO_4$ at a flow rate of 10 or 60 μL min^{-1}. The model predicted maximum power densities of ~35 and ~36 mW cm^{-2} when the cell is operated at a flow rate of 10 and 60 μL min^{-1}, respectively. As elaborated earlier, this slight improvement in power density may be attributed to changes in the depletion region as reactant flow rate is increased. However, the improvement in cell performance is so small that may be required to run this cell at a low flow rate (*i.e.,* 10 μL min^{-1}) to increase reactant residence time within the microchannels, thereby, increasing reactant utilization. Also, the power losses associated with active reactant delivery (*i.e.,* pumps) will increase as the input flow rate increases. To minimize this power loss reactant delivery at low flow rates is preferred. A more detailed discussion on ancillary power losses and reactant utilization is covered in Sections 4.12.3, 4.12.4, and 4.12.5. Also, when comparing AR 10 to AR 5 cell structures, the later shows improvement in cell performance. This improvement is mainly due to the decreased resistance of the cell as we decrease the bridge aspect ratio of the cell.

Figure 4.15 illustrates oxidant (*i.e.,* permanganate) concentration profiles for AR 4 cell structure when fed with 20 mM $KMnO_4$ at a flow rate of 10 or 60 μL min^{-1}. A 3D flow domain is shown in the left upper insert of the figure along with 2D snapshots (x-z planes) located at three different locations from the cell active-channel entrance (1, 5, and 9 mm in the downstream direction) as shown in the left lower insert. For the AR 4 cell structure the model predicted a peak power density of ~ 17 and ~ 31 mW cm^{-2} at a flow rate of 10 and 60 μL min^{-1}, respectively. As in previous cases, an increase in reactant flow rate improves cell performance which is attributed to changes in the depletion regions. Also, an improvement in overall cell performance

at low oxidant concentration (*i.e.,* 20 mM $KMnO_4$) is noted when the bridge aspect ratio decreases from AR = 10 to AR = 4. Decreasing the bridge aspect ratio implies a bigger aperture for protons transport (*i.e.,* increased bridge height) which reduces the cell resistance, thereby, improving cell performance.

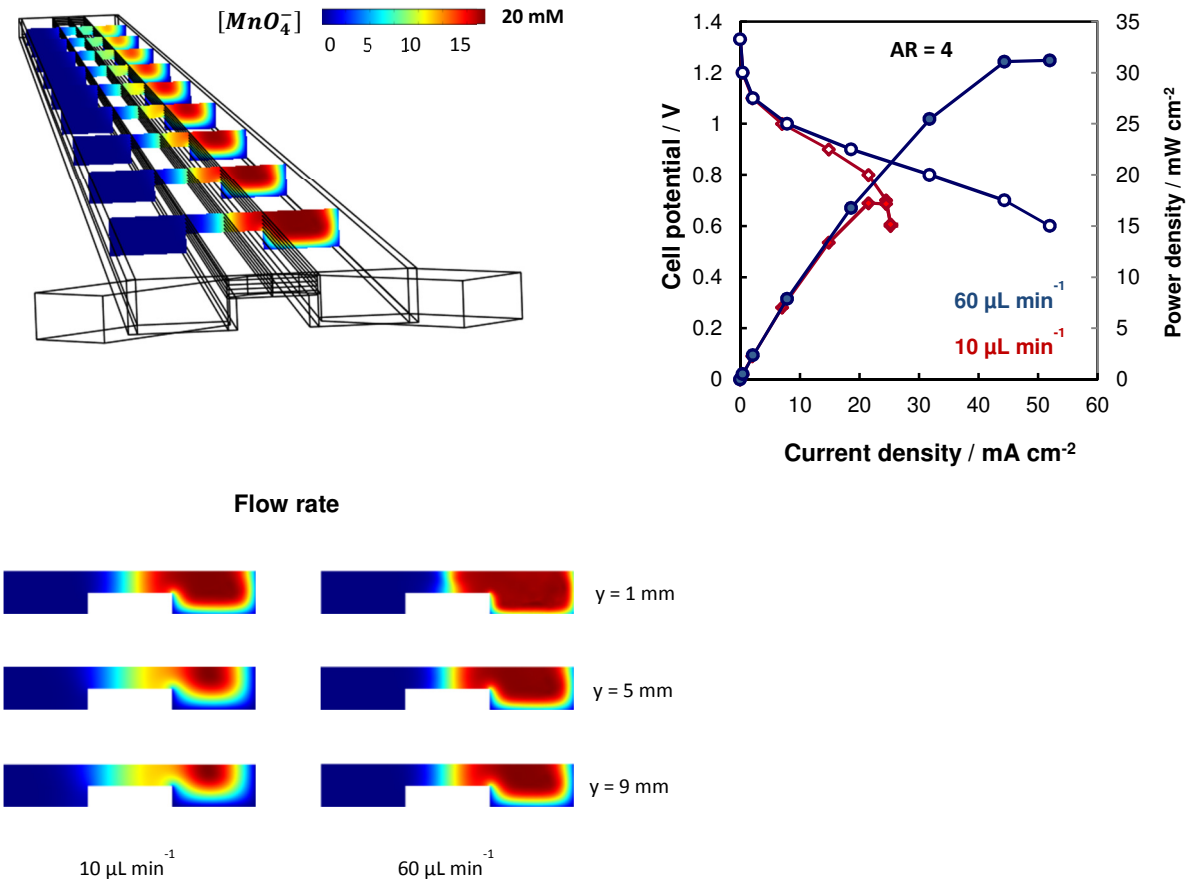

Figure 4.15. COMSOL captures (left inserts): oxidant (*i.e.,* permanganate) concentration profiles for AR 4 cell structure when fed with 20 mM $KMnO_4$ at a flow rate of 10 or 60 µL min^{-1}. The 3D flow domain (left upper insert) and 2D snapshots (left lower insert) with x-z planes located at three different locations from the cell active-channel entrance (1, 5, and 9 mm in the downstream direction). Right upper insert: polarization (open squares and circles) and power-density (filled squares and circles), as predicted by the model.

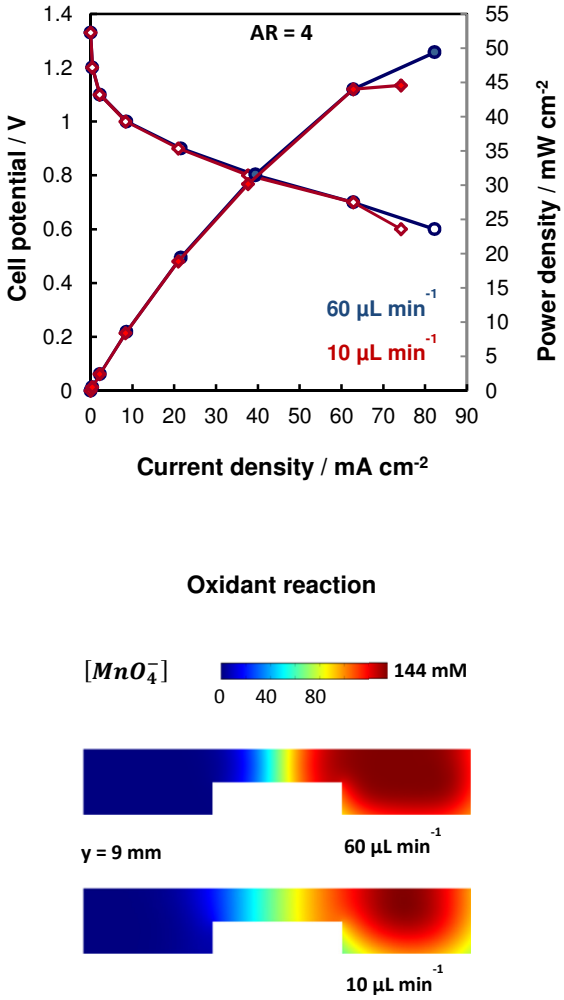

Figure 4.16. Polarization (open squares and circles) and power-density (filled squares and circles) curves for the AR 4 cell structure when operating with 1 M HCOOH and 144 mM $KMnO_4$ at low and high flow rates (10 and 60 µL min^{-1}, respectively) (upper insert). 2-D (x-z) plane snapshot of the oxidant concentration field at a location of y = 9 mm from the active cell entrance (lower insert).

Figure 4.16 (upper plot) shows polarization (open squares and circles) and power-density (filled squares and circles) curves for AR 4 cell structure. The plot shows the performance of this cell when operated with 1 M HCOOH and high oxidant concentration of 144 mM $KMnO_4$ at a flow rate of 10 or 60 µL min^{-1}. The model predicted maximum power densities of ~44 and ~49 mW cm^{-2} when the cell is operated at a flow rate of 10 and 60 µL min^{-1}, respectively. As

aforementioned, this slight improvement in power density may be attributed to changes in the depletion region as reactant flow rate is increased. However, the improvement in cell performance is so small that may be required to run this cell at a low flow rate (*i.e.,* 10 μL min^{-1}) to increase reactant residence time within the microchannels, therefore, increasing reactant utilization. Also, the power losses associated with active reactant delivery (*i.e.,* pumps) will increase as the input flow rate increases. To minimize this power loss reactant delivery at low flow rates is preferred. Also, when comparing AR 10, AR 5, and AR 4 cell structures, the later shows the highest cell performance. This improvement is mainly due to the decreased resistance of the cell as we decrease the bridge aspect ratio of the cell. However, we expect that if we increase the height of the bridge significantly (> 25 μm), the inner reactive walls will be lost, hampering cell performance.

4.12.3 Power Losses

Ancillary

Figure 4.17 shows the power losses due to active reactant delivery (*i.e.,* pump). The data was determined using the pressure drop simulation results for the ranges of reactant flow rates $\dot{V} \in \{10,20,30,40,50,60\}$ μL min^{-1} and the three different aspect ratios (*i.e.,* AR 10, AR 5, and AR 4) considered in our studies.

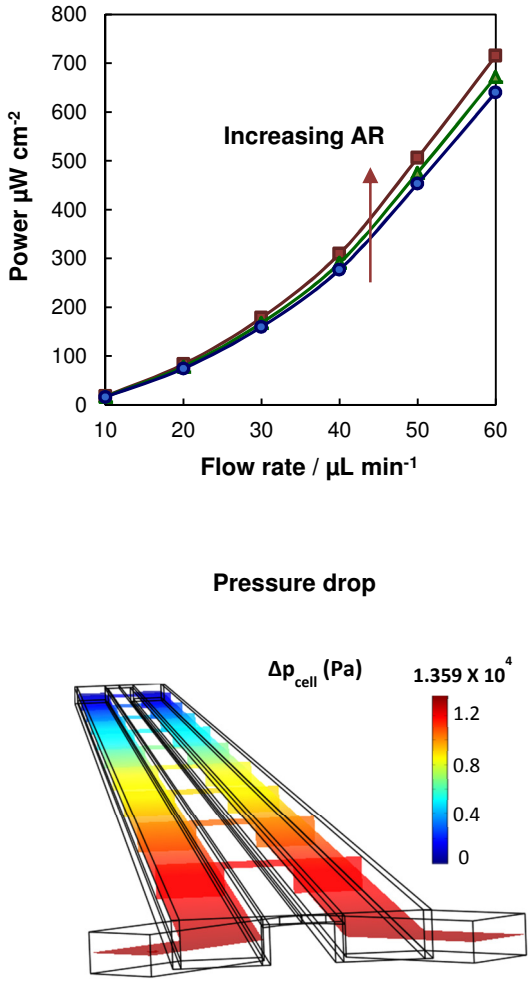

Figure 4.17. Power losses (µW cm^{-2}) due to active reactant delivery (i.e., pump) determined from cell pressure drop for the ranges of reactant flow rates $\dot{V} \in \{10,20,30,40,50,60\}$ µL min^{-1} and the three different aspect ratios (e.i., AR 10, AR 5, and AR 4).

As noted from the figures power losses associated with active reactant delivery increase proportional to flow rate. Since pressure drop is proportional to flow rate, the pump power required is larger. Also, as the aspect ratio of the structure (recall AR = bridge width / bridge height) increases the power losses also increases. Increasing the aspect ratio of the structure implies a more decreased gap height. Therefore, the cross-sectional area of the structure

decreases making the pump of reactants more challenging and, consequently, power consumption.

Crossover / crossover current

Figure 4.18 shows the quantification of crossover current due to oxidant or fuel reactant crossover for the AR 4 structure. AR 4 structure was selected for the analysis since it showed the largest extent of fuel crossover according to the mixing zone model discussed in Section 4.4. The bar data represents the crossover current computed for AR 4 cell operating at V_{cell} = 0.7 V. To obtain this data we have assumed that the amount of fuel that crosses to the cathodic micro flow channel is completely oxidized at the catalyst layer and the amount of oxidant that crosses to the anodic micro flow channel is completely reduced at the catalyst layer.

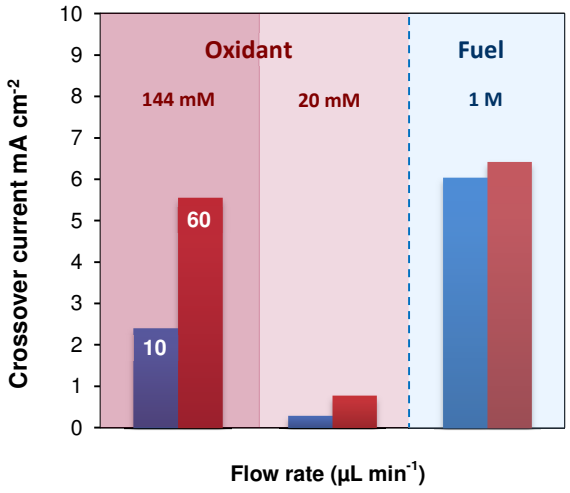

Figure 4.18. Crossover current (mA cm^{-2}) due to oxidant and fuel reactant crossover for AR 4 structure operating at the lowest and highest reactant flow rate (*i.e.,* 10 and 60 µL min^{-1}), lowest and highest oxidant concentration (*i.e.,* 20 and 144 mM, respectively), and fuel concentration of 1 M HCOOH.

When the cell is operating at a fuel and oxidant concentration of 1M HCOOH and 144 mM $KMnO_4$, respectively, with a flow rate of 10 μL min^{-1}, cross over currents of 6 and 2.4 mA cm^{-2} were estimated due to fuel and oxidant crossover, respectively. Similarly when the cell operates under the same conditions at higher reactant flow rate (*i.e.,* 60 μL min^{-1}), crossover currents of 6.4 and 5.5 mA cm^{-2} were measured. Note that the variation of crossover currents due to fuel crossover is not as marked as the variation of crossover current due to oxidant crossover when flow rate is increased from 10 to 60 μL min^{-1}. For the case of high oxidant concentration, when the flow rate is increased crossover current increases significantly. At low flow rates the oxidant depletion region is more pronounced (also oxidant consumption as explained later) lessening the concentration gradient for oxidant cross flux to the anodic micro flow channel. However, the overall trend seems to be a gradual increase of crossover current while increasing flow rate. When the cell operates at the lowest oxidant concentration, very low crossover currents were estimated (0.3 and 0.78 mA cm^{-2} for a flow rate of 10 and 60 μL min^{-1}, respectively). This shows that lowering the reactant concentration is an effective way of reducing crossover and consequent crossover current density. In general, if any of the reactant concentrations is lowered, the gradient across the mixing zone is lessened which decreases the driving force for fuel or oxidant cross flux.

4.12.4 Fuel Utilization (at V_{cell})

Figure 4.19 shows the fuel utilization (in %) for the structure AR 4 when operating with 1M HCOOH at the lowest and highest flow rates selected for our analysis (*i.e.,* 10 and 60 μL min^{-1}). Fuel concentration profiles are shown when the cell operates at the lowest and highest flow rate. The x-z planes are located at y = 9 mm (close to the cell exit) which offers a more apparent fuel depletion region compared to x-z planes located close to the cell entrance.

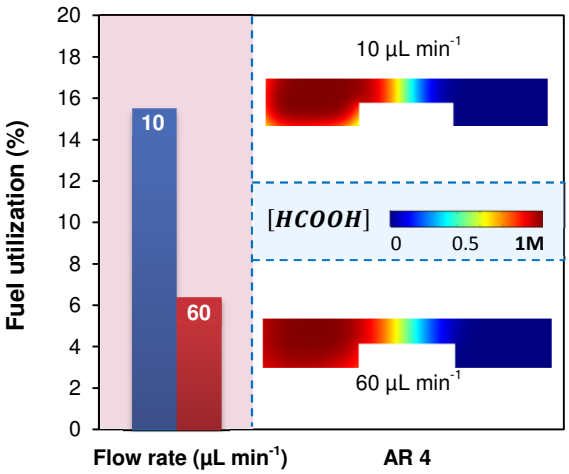

Figure 4.19. Fuel utilization (%) for the AR 4 structure operating with 1M HCOOH at the lowest and highest flow rates (*i.e.,* 10 and 60 µL min^{-1}). Fuel utilization concentration captures are provided for the different flow rates. These x-z planes are located at y = 9 mm (close to the cell exit) which offers are more apparent fuel depletion region compared to x-z planes located close to the cell entrance.

When the cell is operating at the lowest flow rate, the fuel utilization is 15.5 % for an inlet fuel concentration of 1M HCOOH. Similarly, for the highest flow rate, a fuel utilization of 6.4 % is obtained. Here, the lowest flow rate produces increased fuel utilization due to the increased fuel residence within the reactive anodic micro flow channel. On the other hand, operating the micro-fuel cell at the highest reactant flow rate will decrease fuel utilization by ~ 41 %. By inspecting the COMSOL fuel concentration captures for the highest operating flow rate we observe a modest boundary (depletion) layer which explains the low fuel utilization percent obtained under these conditions. A more apparent fuel depletion region is observed for the lowest operating flow rate, which proves the higher fuel utilization percent obtained under these conditions. However, our cell is cathode limited which means that the producing current will balance according to the cathode reaction kinetics. Therefore, the cell cannot be optimized by

increasing fuel concentration but fuel utilization can be greatly improved by decreasing the fuel concentration.

4.12.5 Oxidant Consumption Rate (at V_{cell})

Figure 4.20 shows the oxidant consumption rate (in %) for the structure AR 4 when operating at the lowest and highest reactant flow rate (*i.e.,* 10 and 60 µL min^{-1}, respectively) and lowest and highest oxidant concentration (*i.e.,* 20 and 144 mM, respectively). Oxidant concentration profiles are also shown when the cell operates at the lowest and highest concentration at a common flow rate of 10 µL min^{-1}, which describes a more apparent depletion layer for both each case.

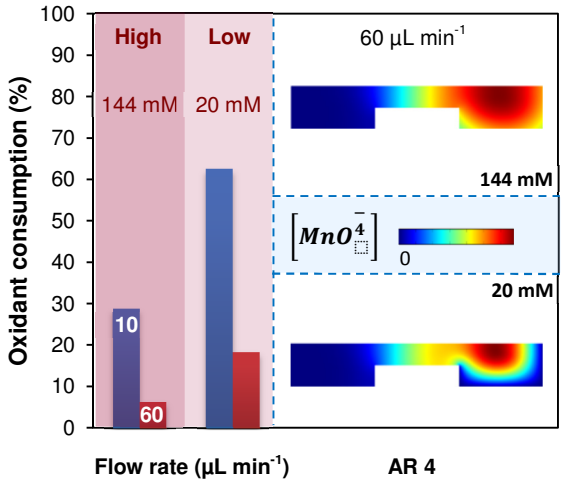

Figure 4.20. Oxidant consumption rate (%) for the AR 4 structure operating at the lowest and highest flow rate (*i.e.,* 10 and 60 µL min^{-1}) and lowest and highest concentration (*i.e.,* 20 and 144 mM, respectively). Oxidant concentration captures are provided for the lowest flow rate (10 µL min^{-1} mM) which describes a more apparent depletion (consumption) layer. These x-z planes are located at y = 9 mm (close to the cell exit).

At the highest and lowest operating concentration, the oxidant consumption is 28 % and 62 %, respectively, for a flow rate of 10 μL min^{-1}. Similarly, the oxidant consumption is 18 % and 6 % when the flow rate is 60 μL min^{-1}. In general, the lowest flow rate produces the major oxidant consumption due to the increased oxidant residence within the reactive cathodic micro flow channel. Also, the lowest oxidant concentration shows increased oxidant consumption in comparison to the highest oxidant concentration. By inspecting the COMSOL oxidant concentration captures for the lowest operating concentration we observe a very deep blue boundary (depletion) layer for a flow rate of 10 μL min^{-1}, which explains the high consumption value obtained under these conditions. This feature explains the marked mass transport limitation shown in the corresponding polarization curve (Section 4.5.2) which is responsible for a decreased performance. A more gradual oxidant depletion layer is observed for the highest operating concentration which produces less oxidant consumption but increased performance in the polarization curve (Section 4.5.2).

4.13 Summary

In this chapter, we have presented a fully-coupled three dimensional numerical model for laminar flow fuel cells (LFFCs) which includes all transport processes and electrochemical phenomena that may occur during operation. The model couples mass, momentum, species, and charge balances along with Butler-Volmer equations for electrode kinetics. Additional modeling efforts were accomplished to determine reactant utilization, reactant crossover and crossover current, and ancillary power losses associated with active reactant delivery (*i.e.,* pumps). The model was validated using the experimental data (*i.e.,* I-V cell performance curves) of a micro laminar flow fuel cell (μLFFC) with a bridge-shaped microchannel cross-section already

reported in literature by the present author [3]. The cell performance predicted via modeling was in close agreement with experimental data. Therefore, the model serves as a virtual tool for performance predictions of LFFCs.

The model was used to optimize the design of an on-chip integrated μLFFC with a bridge-shaped microchannel cross-section [3]. The purpose of employing a bridge-shaped microchannel cross-section for the μLFFC was twofold: to reduce the fuel-to-oxidant interfacial contact, thereby, minimizing reactant crossover and to isolate the evolving mixing zone from the reactive walls. Minimizing reactant crossover and achieving separation of the mixing and reactions zones may increase reactant utilization and improve cell performance. In our analysis, three cell structures with different bridge height (AR 10, AR 5, and AR 4) were built using the commercial finite-element-method software COMSOL Multiphysics. First, a simplified version of the model was developed, namely, the mixing zone model, to study the behavior of the mixing zone upon bridge geometrical modifications and upstream flow conditions. The model suggested the use of high flow rates to confine the mixing zone along the bridge for the entire flow domain and avoid its interaction with the electrode walls during operation. A similar trend is noted by opening the bridge structure (*i.e.,* decreasing the bridge aspect ratio). However, the modeling data shows that opening the cell structure may cause fuel crossover up to 1.2 % (for AR 4 cell) when operated with 1M HCOOH at low flow rate (10 μL min^{-1}). Second, a complete version of the model was developed, namely, the fuel cell model, to couple the chain of transport and electrochemical phenomena that occur within the operating cell structures to analyze the impact on net cell performance. For the structures studied herein, AR 4 was found to produce the higher power output (~49 mW cm^{-2}) when operated with 1M HCOOH and 144 mM $KMnO_4$. The cell is preferably operated at low flow rates (e.g., 10 μL min^{-1}) which improves reactant utilization,

minimizes power losses associated with active reactant delivery (i.e., pumps) and produces the less crossover current densities as elaborated in Sections 4.12.3 – 4.12.5.

4.14 References

[1] Bazylak, A., Sinton, D. & Djilali, N. 2005, "Improved fuel utilization in microfluidic fuel cells: A computational study", *Journal of Power Sources,* vol. 143, no. 1-2, pp. 57-66.

[2] Chang, M.-H., Chen, F. & Fang, N.-. 2006, "Analysis of membraneless fuel cell using laminar flow in a Y-shaped microchannel", *Journal of Power Sources,* vol. 159, no. 2, pp. 810-816.

[3] López-Montesinos, P.O., Yossakda, N., Schmidt, A., Brushett, F.R., Pelton, W.E. & Kenis, P.J.A. 2011, "Design, fabrication, and characterization of a planar, silicon-based, monolithically integrated micro laminar flow fuel cell with a bridge-shaped microchannel cross-section", *Journal of Power Sources,* vol. 196, no. 10, pp. 4638-4645.

[4] Lee, S.J., Chang-Chien, A., Cha, S.W., O'Hayre, R., Park, Y.I., Saito, Y. & Prinz, F.B. 2002, "Design and fabrication of a micro fuel cell array with "flip-flop" interconnection", *Journal of Power Sources,* vol. 112, no. 2, pp. 410-418.

[5] Motokawa, S., Mohamedi, M., Momma, T., Shoji, S. & Osaka, T. 2004, "MEMS-based design and fabrication of a new concept micro direct methanol fuel cell (μ-DMFC)", *Electrochemistry Communications,* vol. 6, no. 6, pp. 562-565.

[6] Min, K., Tanaka, S. & Esashi, M. 2006, "Fabrication of novel MEMS-based polymer electrolyte fuel cell architectures with catalytic electrodes supported on porous SiO2", *Journal of Micromechanics and Microengineering,* vol. 16, no. 3, pp. 505-511.

[7] Xiao, Z., Feng, C., Chan, P.C.H. & Hsing, I.-. 2008, "Monolithically integrated planar microfuel cell arrays", *Sensors and Actuators, B: Chemical,* vol. 132, no. 2, pp. 576-586.

[8] Tominaka, S., Ohta, S., Obata, H., Momma, T. & Osaka, T. 2008, "On-chip fuel cell: Micro direct methanol fuel cell of an air-breathing, membraneless, and monolithic design", *Journal of the American Chemical Society,* vol. 130, no. 32, pp. 10456-10457.

[9] Shen, M., Walter, S. & Gijs, M.A.M. 2009, "Monolithic micro-direct methanol fuel cell in polydimethylsiloxane with microfluidic channel-integrated Nafion strip", *Journal of Power Sources,* vol. 193, no. 2, pp. 761-765.

[10] Frank, M., Erdler, G., Frerichs, H.-., Müller, C. & Reinecke, H. 2008, "Chip integrated fuel cell accumulator", *Journal of Power Sources,* vol. 181, no. 2, pp. 371-377.

[11] Moore, C.W., Li, J. & Kohl, P.A. 2005, "Microfabricated fuel cells with thin-film silicon dioxide proton exchange membranes", *Journal of the Electrochemical Society,* vol. 152, no. 8, pp. A1606-A1612.

[12] Choban, E.R., Markoski, L.J., Stoltzfus, J., Moore, J.S. & Kenis, P.J.A. 2002, "Microfluidic Fuel Cells that Lack a PEM", *Power Sources Proceedings*, vol. 40, 317-320.

[13] Choban, E.R., Markoski, L.J., Wieckowski, A. & Kenis, P.J.A. 2004, "Microfluidic fuel cell based on laminar flow", *Journal of Power Sources,* vol. 128, no. 1, pp. 54-60.

[14] Ismagilov, R.F., Stroock, A.D., Kenis, P.J.A., Whitesides, G. & Stone, H.A. 2000, "Experimental and theoretical scaling laws for transverse diffusive broadening in two-phase laminar flows in microchannels", *Applied Physics Letters,* vol. 76, no. 17, pp. 2376-2378.

[15] Ahmed, D.H., Park, H.B. & Sung, H.J. 2008, "Optimum geometrical design for improved fuel utilization in membraneless micro fuel cell", Journal of Power Sources, vol. 185, no. 1, pp. 143-152.

[16] Park, H.B., Ahmed, D.H., Lee, K.H. & Sung, H.J. 2009, "An H-shaped design for membraneless micro fuel cells", *Electrochimica Acta,* vol. 54, no. 18, pp. 4416-4425.

Chapter 5

Summary of Accomplishments

In this work, approaches to monolithic integration of micro-fuel cells were investigated. MEMS-based / CMOS-compatible fabrication lines that include high surface area catalyst integration were developed to achieve on-chip micro-fuel cell integration. 3-D computational numerical modeling was performed to further study, characterize, and optimize micro laminar flow fuel cells.

In brief, we have fabricated a planar, silicon-based, monolithically integrated, μLFFC suitable as an on-chip power source. The MEMS-based, IC-compatible (*i.e.,* CMOS-compatible) fabrication line of these cells may facilitate their integration with other components and controlling electronics on the same chip. A new bridge-shaped microchannel cross-section was explored to reduce fuel-to-oxidant interfacial contact (thereby, minimizing reactant crossover) and separate the mixing and reaction zones over the entire flow domain to enhance reactant transport to the electrodes and improve fuel utilization and overall performance. On-chip integration of power sources may foster overall device miniaturization, weight and cost reduction, batch production, and reproducibility as desired for commercial interests. The planar, membraneless, monolithic, and CMOS-compatible micro-fuel cell design presented in this thesis may offer a solution to the next generation of MEMS and consumer electronics whose highly integrated platforms demand on-chip incorporation of the power source.

In this work, we have also developed a fully-coupled 3-D computational numerical model for laminar flow fuel cells (LFFCs) which includes all transport processes and electrochemical phenomena that may occur during operation. The model couples mass, momentum, species, and

charge balances along with Butler-Volmer equations for electrode kinetics. Additional modeling efforts were accomplished to determine reactant utilization, reactant crossover and crossover current, and ancillary power losses associated with active reactant delivery (*i.e.,* pumps). The model was validated using the experimental data (*i.e.,* I-V cell performance curves) of a micro laminar flow fuel cell (μLFFC) with a bridge-shaped microchannel cross-section already reported in literature by the present author [3]. The cell performance predicted via modeling was in close agreement with experimental data. The model presented here serves as a virtual tool for performance predictions of LFFCs in general.

Appendix A

Table A.1. Input parameters used in the model*

Property	Symbol	Value	Units
Anode exchange current density	i_{0_a}	0.46	A m^{-2}
Anode overpotential	η_a		V
Anode reversible potential	φ_{rev_a}	-0.7	V
Anodic charge transfer coefficient of the oxidation reaction at the anode	$\propto_{a_a}$	0.5	-
Anodic charge transfer coefficient of the reaction at the cathode electrode	$\propto_{a_c}$	0.5	-
Average flow velocity	U_y		m s^{-1}
Body-force vector	**b**		N
Cathode exchange current density	i_{0_c}	0.46	A m^{-2}
Cathode overpotential	η_c		V
Cathode reversible potential	φ_{rev_c}	1.33	V
Cathodic charge transfer coefficient of the reaction at the anode electrode	$\propto_{c_a}$	0.5	-
Cathodic charge transfer coefficient of the reaction at the cathode electrode	$\propto_{c_c}$	0.5	-
Cell pressure drop (AR 10)	Δp_{cell}	{2033, 4747, 6784, 8822, 11540, 13590}	N m^{-2}
Concentration of a species	c		mol m^{-3}
Conductivity	σ		S m^{-1}
Crossover current due to fuel crossover	I_{co_f}		A
Crossover current due to oxidant crossover	I_{co_o}		A
Current generated at the anode	I_a		A
Current generated at the cathode	I_c		A
Current vector	**J**		A
Density of the fluids	ρ	1000	Kg m^{-3}
Diffusivity of fuel	D_{HCOOH}	$5x10^{-10}$	m^2 s^{-1}
Diffusivity of the species	D		m^2 s^{-1}

* Values acquired from the literature (offered in Section 4.14)

Table A.1 (cont.)

Effective conductivity	σ_{eff}		S m^{-1}
Electrical conductivity of liquid electrolyte in anodic microchanel	σ_{e_a}	3.5	S m^{-1}
Electrical conductivity of liquid Electrolyte in cathodic microchannel	σ_{e_c}	3.5	S m^{-1}
Electrical conductivity of non-porous material (Pd)	σ_0	10 x 10^6	S m^{-1}
Electrical current source term	S_φ		A m^{-3}
Electrochemical surface area	A_s		m^2
Faraday constant	F	96485	C
Flow rate	$\dot{V}$	{10, 20, 30, 40, 50, 60}	µL·min^{-1}
Fluid viscosity	μ	1e10^{-3}	Kg m^{-1} s^{-1}
Flux vector	**N**		mol m^{-2} s^{-2}
Flux of fuel or oxidant	N_0		mol m^{-2} s^{-2}
Fuel and oxidant inlet velocity	u	{30, 70, 100, 130, 170, 200}	mm s^{-1}
Fuel inlet molar flow rate	$\dot{n}_{f\,in}$		mol s^{-1}
Fuel outlet molar flow rate	$\dot{n}_{f\,out}$		mol s^{-1}
Fuel utilization	Ω		%
Height of the channel	H		µm
Ideal gas constant	R	8.314	J mol^{-1} K^{-1}
Inlet concentration	c_{in}	1000	mol·m^{-3}
Inlet pressure	p_{in}		N m^{-2}
Local liquid-phase potential	φ_e		V
Local normal flux	$F_\perp$		mol m^{-2} s^{-2}
Local potential	ϕ		V
Magnitude of the velocity component in the flow direction	v_y		m s^{-1}
Molar flux of fuel crossover	M_f		mol m^{-2} s^{-2}
Molar flux of oxidant crossover	M_o		mol m^{-2} s^{-2}
Normal current generated at the anode	J_{n_a}		A
Normal current generated at the cathode	J_{n_c}		A
Normal current at the electrode surface	J_n		A
Normal vector	**n**		-
Number of electrons involved in the	N_{e_o}	2	-

Table A.1 (cont.)

oxidation reaction			
Number of electrons involved in reduction reaction	N_{e_r}	3	-
Number of moles	n		-
Operating cell voltage	V_{cell}		V
Oxidant consumption rate	λ		%
Oxidant inlet molar flow rate	$\dot{n}_{o\,in}$		mol s^{-1}
Oxidant outlet molar flow rate	$\dot{n}_{o\,out}$		mol s^{-1}
Péclet number	Pe		-
Porosity of the catalyst	ε	0.4	-
Pressure	P		N m^{-2}
Ratio of the bridge width to the bridge height	AR		-
Reference concentration	c_{ref}		mol m^{-3}
Solid-phase local potential	φ_s		V
Temperature	T	298	K
Velocity vector	**u**		m s^{-1}
Width of mixing zone	Δx		μm